RESOLVING THE SMALL-SCALE SPATIAL CURRENT STRUCTURE OF THE UPPER TEXAS COAST

A Thesis

by

LUZ ARELI ZARATE JIMENEZ

Submitted to the Office of Graduate and Professional Studies of
Texas A&M University
in partial fulfillment of the requirements for the degree of

MASTER OF SCIENCE

Chair of Committee,	Steven F. DiMarco
Committee Members,	Courtney Schumacher
	Henry Potter
Head of Department,	Shari Yvon-Lewis

August 2018

Major Subject: Oceanography

ABSTRACT

Understanding the circulation of the oceanic currents provides information to mitigate the impact of hazards and to respond timely in the case of an emergency by making critical decisions promptly. In early 2016, the Geochemical and Environmental Research Group (GERG) started the installation of a High-Frequency (HF) radar network in Texas to improve the spatial resolution of the in situ oceanic measurements presently collected by the Texas Automated Buoy System (TABS). Both systems, HF radar and TABS, are operated and maintained by GERG. The present research thesis analyzes 2 out of the 3 HF radar sites (Rollover and Surfside), and 4 out of the 9 TABS buoys (B, F, W, and R), for a period of ~17.5 months, from June of 2016-November of 2017. During this analysis the summer reversal for 2016 and 2017 is captured, noting that it occurred in mid-June – mid-August, and a few days earlier in 2016. Based on correlation coefficients, SSDE performs better than RLVR, particularly when compared to buoy F. Bathymetry and salinity impact the performance of the HF radar, and there is potential attenuation on RLVR by ship navigation. Variance ellipses tend to follow the 50-m isobath, in agreement to Nowlin et al. (2005) inshore-offshore isobath limit definition, with a dominant NE-SW orientation of the major axis, with a higher variance associated with regions of less data density and steeper gradients in the bathymetry. Power spectra showed an increase in the energy in the diurnal and semidiurnal frequency, with a predominant clockwise rotation as indicated by rotary spectra. Coherence analysis showed coherence >95% confidence interval near the inertial band is indicative of rotation due to inertial response. The main tidal constituents found in this thesis are O1,

P1, K1, M2, and S2. Wavelet analysis also showed an increase in the diurnal and semi-diurnal period, as well as an increase in the energy in the weather band (2-15 days), and high power content on the diurnal band during the summer for the detided record, suggesting that this is due to sea-breeze effects and inertial motions, given that the local inertial period is 24.78 hrs.

DEDICATION

To the effort of my parents

ACKNOWLEDGEMENTS

I would like to thank my committee chair, Dr. Steven DiMarco, and my committee members, Dr. Henry Potter, and Dr. Courtney Schumacher, for their guidance throughout the course of this research. Special thanks to Dr. Kerri Whilden for her engagement on this project.

I would like to thank Dr. DiMarco for his endless support. Dr. DiMarco granted me with his trust and enabled me the opportunity to advance my education in his research group, providing me with the peace of mind of having secure funding, as well as the opportunity of broadening my formation by participating on fieldwork experiences (oceanographic campaigns and an aerial surveillance project), conferences, and workshops. I will always owe Dr. DiMarco, and my respect for him will remain forever.

I would like to thank the Society for Underwater Technology (SUT) for being a liaison between academia and industry. I have learned, grown, built connections and benefited from a competitive scholarship through this society. I would like to thank the Global Ocean Ship-based Hydrographic Investigations Program (GO–SHIP) for allowing me to collaborate in a cruise along the Pacific 32°S hydrographic line. Especially, I want to extend my thankfulness to Dr. Kevin Speer, Chief Scientist on the leg 2.

I take this opportunity to extend my thankfulness to the Mexican National Council of Science and Technology (CONACyT), the Marine Technology Society (MTS), Texas Sea Grant, and the Department of Oceanography for providing additional funding for the completion of my degree.

CONTRIBUTORS AND FUNDING SOURCES

Contributors

This work was supervised by a thesis committee consisting of Professor Dr. Steven F. DiMarco and Dr. Henry Potter of the Department of Oceanography, and Dr. Courtney Schumacher of the Department of Atmospheric Sciences.

The installation and land use authorization process for the high-frequency radar antennas has been possible through the joint effort of Dr. Steven DiMarco, Dr. Anthony Knap, John Walpert, Dr. Kerri Whilden and Andrew Dancer. Dr. DiMarco and Dr. Whilden made important contributions on the technical aspects of the data processing.

The Texas General Land Office (Contract No. 16–097–000–9289) and the Texas A&M System, through the Chancellor's Research Initiative, funded this research.

Funding Sources

Funding for the graduate education was provided with an appointment as Graduate Research Assistant since September of 2015 with one semester as Graduate Teaching Assistant through the Department of Oceanography. Additional funding was granted through the Mexican National Council of Science and Technology (CONACyT), James Sharp Graduate Competitive Scholarship, Global Ocean Ship-based Hydrographic Investigation Program (GO-SHIP), Ross, Donald & Melba Graduate School Scholarship, Texas Sea Grant Rayburn Scholarship, Marine Technology Society Scholarship for Graduate Students, and the Society for Underwater Technology Scholarship.

NOMENCLATURE

ANWR	Aransas National Wildlife Refuge
CODAR	Coastal Ocean Dynamics Applications Radar
c.p.d	Cycles Per Day
DCS	Doppler Current Sensor
DFT	Discrete Fourier Transform
E	East
EEZ	Economic Exclusive Zone
GCOOS	Gulf of Mexico Coastal Ocean Observing Systm
GERG	Geochemical and Environmental Research Group
GoM	Gulf of Mexico
HF	High-Frequency
IOOS	Integrated Ocean Observing Systems
LATEX	Texas-Louisiana
MBNP	Matagorda Bay Nature Park
MCD	Method of Cyclic Descent
NOAA	National Oceanic and Atmospheric Administration
N	North
NE	Northeast
NW	Northwest
TGLO	Texas General Land Office
TABS	Texas Automated Buoy System

TAMU	Texas A&M University
OOS	Ocean Observing System
PINS	Padre Island National Seashore
PMPI	Port Mansfield Padre Island
RLVR	Rollover Pass
SAR	Search and Rescue
S	South
SE	Southeast
SW	Southwest
SSDE	Surfside Beach
USCG	U.S. Coast Guard
UTC	Coordinated Universal Time
W	West

TABLE OF CONTENTS

Page

Page

LIST OF FIGURES

Page

Page

Page

LIST OF TABLES

Page

1. INTRODUCTION*

1.1 General Circulation of the Gulf of Mexico

The Gulf of Mexico (GoM) is a semi-enclosed basin that covers an area of $1.6x10^6$ km^2 and stores a volume of 2.3 x 10^6 km^3, with a central depth basin of approximately 3500 m, with its deepest location corresponds to the Sigsbee Escarpment. The GoM receives Caribbean waters through the Yucatan Channel. Once the water enters into the GoM, it forms the Loop Current (LC) that later exits as the Florida Current, connecting with the Gulf Stream through the Florida Strait (Nowlin 1971; Oey et al. 2005). The principal forcing mechanisms that drive the large-scale low-frequency motions are the dynamics of the LC system, winds, and tides (Schmitz et al. 2005). Li et al. (1997) defined that river discharge from the Mississippi-Atchafalaya system is an additional forcing on the Texas-Louisiana shelf, hereafter denominated the LATEX shelf. The cross-shelf scales of variability on the Texas coast are 15 km, increasing to up to 20 km to the east of the LATEX shelf (Li et al. 1996).

The LC has an anticyclonic circulation and travels with an average velocity of 0.8 m/s, with peak velocities of 2 m/s transporting 24 Sv (1 Sv = 10^6 m^3/s) (Athié et al. 2015). Related to the LC, there is eddy (closed current vortex) formation and separation, processes that together take between 3–17 months. The eddy separation is known as eddy detachment (Nowlin 1968) and has characteristic separation peaks every 6 and 11 months

---

*Part of this chapter is reprinted with permission from "A high-frequency radar oceanic current monitoring system for the Texas coast." by Zarate, L., DiMarco, S. F., Knap, A., Walpert, J., & Whilden, K. A., 2016. *OCEANS 2016 MTS/IEEE Monterey* (pp. 1-7): IEEE

but it is unusual during the winter (Nowlin et al. 1998; Sturges and Leben 2000). When eddies detach from the LC, they are called Loop Current Eddies (LCE) (Donohue et al. 2016). The LCE have diameters of ~250 km, and usually travel towards the northwest of the GoM with swirl velocities greater than 2 m/s and translational velocities between 2–5 km/day. These eddies can prevail for extended periods of time, on average 9–11 months, until they decay in the northwest GoM (Morey et al. 2003; Schmitz et al. 2005; Zavala-Hidalgo et al. 2006), in the so-called eddy graveyard (Biggs et al. 1996). The LC/LCE's have the potential of impacting the LATEX circulation (Nowlin et al. 2005).Wind curl may modulate the LCE and their interaction with the western boundary, while the flow carried by these eddies is perturbed by the interaction with topographic features and other eddies (Nowlin et al. 1998). Figure 1 depicts the principal physical elements of the GoM.

Cochrane and Kelly (1986) hypothesized that the seasonality of the circulation on the inner LATEX shelf has a predominant downcoast circulation (from Louisiana to Texas) during the non-summer months, late August through June, and an upcoast circulation (from the Mexican shelf to Texas) in July–August. *In situ* observations have confirmed that the low-frequency seasonal variability in the inner LATEX shelf is driven by the along-shelf wind stress (Cho et al. 1998; Wang et al. 1998).

The Intertropical Convergence Zone (ITCZ) is the convergence of the northeast and southeast trade winds. The ITCZ is deepened into the GoM during the summer and dictates the climatology of the GoM. Near to the shore on the LATEX shelf the mean easterly winds have intensities below 1 m/s south of the Mississippi River Delta, increasing westward, to more than 3 m/s off the south Texas coast, showing uniform wind speeds of about 2 m/s over the open GoM (Wang et al. 1998). The flow response to

wind forcing was estimated to reach 100 km scale (Smith 1980), but drifter data records have proven that there is coherent flow response to wind forcing over 600 km scales (Barron and Vastano 1994).

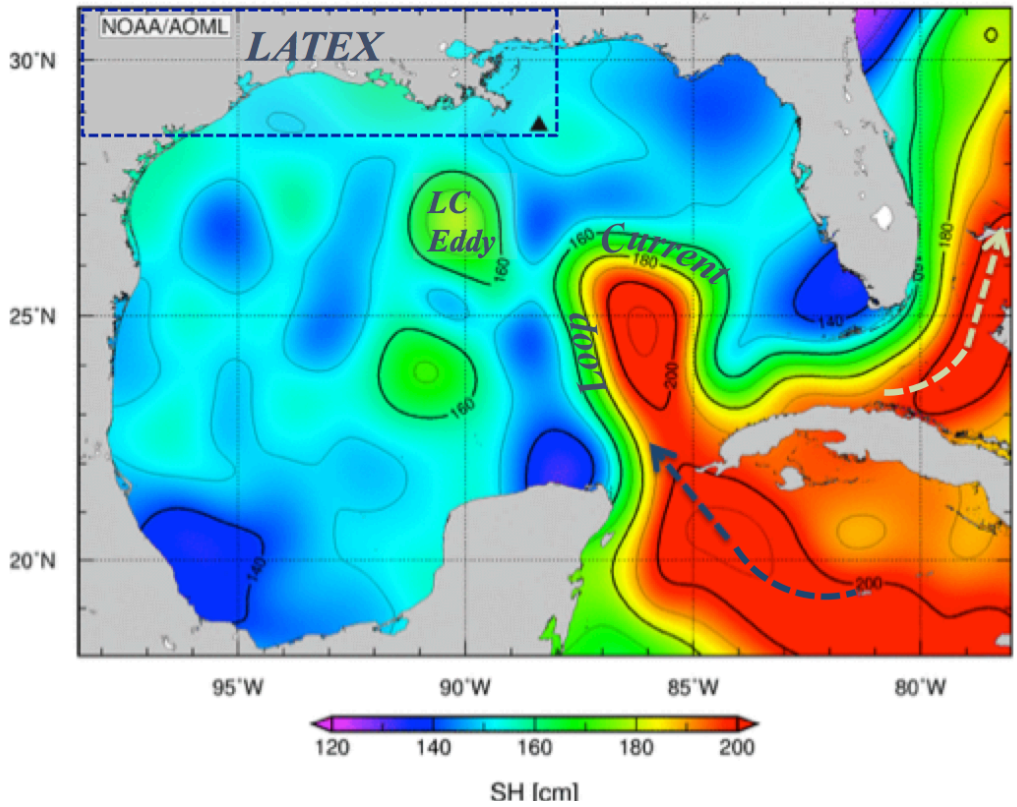

Figure 1. The sea surface height (SSH) imagery depicts the principal circulation features of the Gulf of Mexico and the LATEX shelf (dashed blue box on the northwest Gulf of Mexico). In the interior of the Gulf of Mexico, the Loop Current and an eddy detached from it are shown in the interior of the basin. The entrances to the world oceans are the Yucatan Channel (blue) and the Florida Straits (green). The contours represent changes in surface height (SH), where red (blue) represents greater (lower) heights. Adapted from http://www.aoml.noaa.gov/phod/dhos/altimetry.php.

During the summer (June–August), alongshore winds have a component directed upcoast, ranging from 1–6 m/s (Wang et al. 1998) bringing saline water from Mexico to the Texas shelf (Etter et al. 2004). In early June there is a wind reversal, returning to

downcoast in September. During the non-summer months (September–May), alongshore winds are directed downcoast, freshening the continental shelf by advecting half of the long-term water from the Mississippi River (Etter et al. 2004). During the fall (September–November) and winter (December–February) winds are more variable due to frontal passages. There is an increase in frontal passages frequency during September and October, reaching a maximum of up to 15 passages per month in midwinter, to less than one per month during the summer (Nowlin et al. 1998; Wang et al. 1998, (DiMego et al. 1976)). Figure 2 shows the seasonal variations of the wind stress.

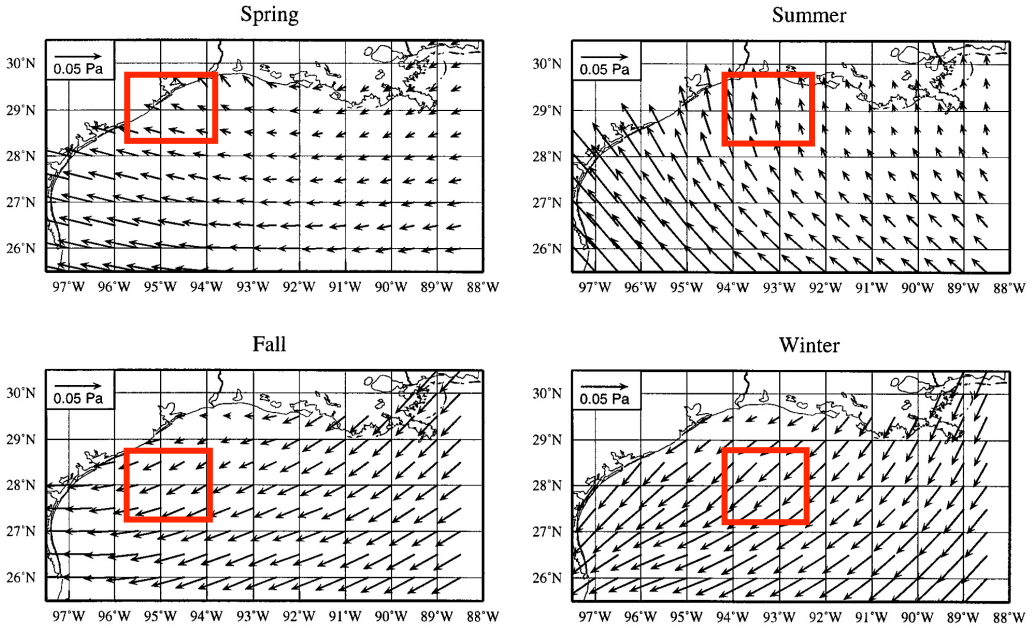

Figure 2. Seasonal mean wind stress fields on the LATEX shelf, constructed from hourly gridded winds for the period of April 1992–November 1994. The arrows indicate the direction and intensity of the wind. The red rectangle represents the study area of the present project. Reprinted and adapted from Wang, Nowlin et al. (1998).

River discharge creates a salinity gradient. The Mississippi-Atchafalaya dominates the annual cycle of river discharge on the LATEX shelf (Dinnel and Wiseman

1986), with influence as far west as Port Aransas due to the downcoast circulation (Smith 1980). The smallest salinity water occurs during April–May when the Mississippi-Atchafalaya discharge peaks (Nowlin et al. 2005), with a maximum freshwater content during May along LATEX (ne and Kelly 1986). Freshening of the western shelf occurs from October–May when the circulation is downcoast. Conversely, the eastern shelf freshens during summer, due to upcoast wind forcing (Nowlin et al. 2005). Figure 3 represents the salinity distribution along the LATEX shelf during the spring (March–May).

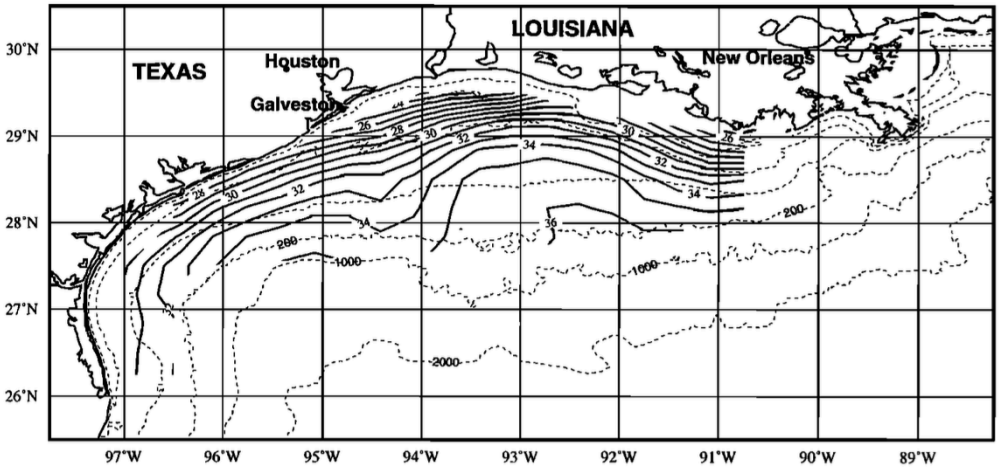

Figure 3. Average sea surface salinity isohalines during spring on the LATEX shelf. Reprinted from Li et al. (1997).

During the fall, the freshwater input is the smallest, with discontinuous alongshore freshwater distribution patterns, where the cross-shelf salinity gradient is smaller, showing a parallel trend between the isobaths and isohalines. October is the month of minimum average discharge throughout the year. During winter (December–

February), there is low freshwater content on the shelf, and February is the month with the smallest freshwater volume of this season. The greatest relative salinity forms a narrow band along the inner shelf (Dinnel and Wiseman 1986; Li et al. 1997).

Astronomical tides influence the horizontal and vertical mixing. DiMarco and O'Reid (1998) analyzed the principal diurnal, 1 c.p.d (O1, K1, P1, and Q1), and semidiurnal, 2 c.p.d (S2, M2, K2, and N2), tidal constituents on the LATEX shelf for a non-summer period. DiMarco and O'Reid (1998) found that the main tidal constituents are O1, K1, and M2, noticing that the diurnal constituents tend to be in phase across and along the shelf (Figure 4), as previously observed by Zetler and Hansen (1970), while the semi-diurnal tides propagate cyclonically westward around the GoM basin. The diurnal tides co-oscillate through the Florida Strait and the Yucatan Channel (Zetler and Hansen 1970), and the semi-diurnal tides propagate around an amphidrome point near the Yucatan shelf (Reid and Whitaker 1981)

Tides in the GoM are considered to be small, particularly the semidiurnal tides, compared to tides around the world. M2, the dominant semi-diurnal tide along the LATEX shelf, has the largest amplitude on the West Florida shelf and secondary maxima near Galveston, Texas (Reid and Whitaker 1981). Near-surface near-shelf tidal currents are between 1–2 cm/s. The magnitude of the tidal amplitude decreases with depth, and the semi-diurnal constituents are amplified further offshore (DiMarco and Reid 1998).

Differential heating and cooling between the ocean and the earth lead to a diurnal sea-breeze that is intensified during the summer months due to the lack of frontal passages. The diurnal sea-breeze produces 24-hour period current oscillations near the surface due to persistent clockwise diurnal wind forcing, resulting in diurnal currents of

up to 60 cm/s, i.e., the largest non-storm induced currents on the shelf (DiMarco et al. 2000; Zhang et al. 2009). The diurnal effect of the sea-breeze along with the inertial period within the latitude range of the GoM, between 24.36–25.31 s^{-1} for this study, produces a near-resonant response to the wind stress (Zhang et al. 2009). On the LATEX shelf, tides account for 10% of the variance up to close to 50% inshore in the inertial band (8 to 40 hour band) (DiMarco 1998).

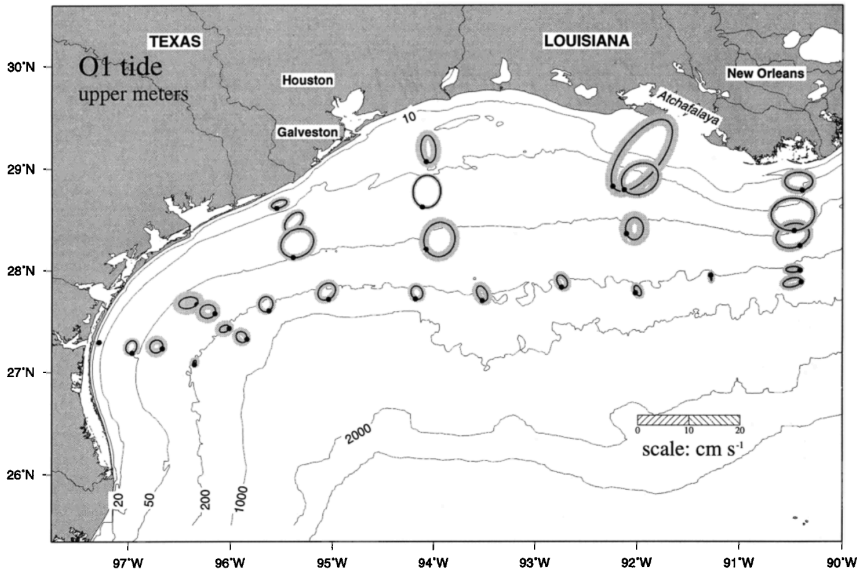

Figure 4. Map representing the mean O1 diurnal tidal current ellipses for the period of April 1992–December 1994. The solid circle indicates the orientation and the shading represents the least squares error estimate. Reprinted from DiMarco and Reid (1998).

1.2 Study Motivation

Based on the report from the Bureau of Ocean Energy Management, as of June of 2018 the Outer Continental Shelf (OCS) of the Gulf of Mexico has a total of 29,000 blocks covering an area of nearly 55,000 km^2. As of 2015, the United States manages

8,000 active oil and gas leases covering an area of nearly 146,000 km^2 on the OCS, with the coast of the GoM and western coast of the USA accounting for 97% of the OCS oil and gas leases in the USA, ~ 24% of the US national oil production (*http://www.boem.gov/uploadedFiles/BOEM/Oil_and_Gas_Energy_Program/Leasing/5BOEMRE_Leasing101.pdf*).

Additionally, there is $20 billion worth estimate of the GoM tourism industry *(https://www.gulfbase.org/environmental–issue/tourism),* and an $818 million revenue form landings of the fisheries industry in the GoM. Louisiana and Texas are the GoM states with highest revenues (*https://www.st.nmfs.noaa.gov/Assets/economics/documents/feus/2011/FEUS2011%20–%20Gulf%20of%20Mexico.pdf).* After the Deepwater Horizon (DWH) oil spill occurred off the coast of Louisiana in 2010, there is a proven necessity of being prepared to respond and provide data to the decision-makers to mitigate the damages after an emergency such as the DWH oil spill. The abundance of oil and gas platforms along the Texas coast represents a high risk for the inhabitants of the coastal regions, and marine and coastal ecosystems.

Since 1996 the Texas Automated Buoy System (TABS) has provided *in situ* atmospheric and oceanic measurements in near-real time at eight locations along the Texas coast. TABS is managed and operated by the Geochemical and Environmental Research Group (GERG) at Texas A&M University, and is funded by the Texas General Land Office (TGLO). The purpose of TABS is to provide information to responders that is useful for the mitigation of the impact of natural hazards like tropical storms and to respond to disasters such as oil spills. Despite the coverage of TABS, 6 long-range high-

frequency (HF) radar, managed and operated by GERG, could improve and supplement the spatial and temporal resolution of TABS. The long-range HF radars measure hourly the speed and direction of the ocean surface currents at a radius up to 200 km with a 6 km resolution (Zarate et al. 2016).

The US has deployed a national HF radar network, with coverage that includes the USA east and west coasts, part of the GoM, Hawaii and Puerto Rico. The Integrated Ocean Observing System (IOOS), a multidisciplinary program designed to compile and distribute oceanographic data to the stakeholders (https://ioos.noaa.gov/), manages the USA national HF radar network (Zarate et al. 2016).

1.3 Study Questions

The current thesis will compare and analyze surface oceanic currents data collected with *in situ* moored current meters and a HF coastal radar system during the period of June, 2016–November, 2017. The study focuses on assessing the performance of the HF radar, as well as a describing the spatial and temporal scales of variability along the upper Texas coast. The questions that drive this research project are:

1) What is the correlation between the surface currents measurements provided by the HF radar and the measurements from the TABS buoys within the footprint of the radar?

To assess the performance of the recently installed HF radar, this project presents the comparison of the data collected by the HF radar with that of the TABS system. A high correlation between the measurements provided by the HF radar and the TABS buoys could result in the implementation of some of the applications performed on other coasts. Some of these applications on the California coast, region with large experience

on HF radar applications, include the creation of a comprehensive program as part of the pollutant tracking, and description of migratory paths of regional larvae (Harlan et al. 2010; Roarty et al. 2010). A weak correlation could be the result of instrumentation issues (calibration), environmental impact (atmospheric refraction), or noise added through anthropogenic activity nearby the antenna (signal attenuation due to interference caused by metal structures such as oil and gas platforms).

2) What are the seasonal variations on how far the HF radar can collect measurements offshore (range)?

The HF radar tends to lose propagation over fresh water, and the signal is enhanced over salty water (Gurgel et al. 1999). The current coverage of the HF radar extends around the Galveston area. Based on Cochrane and Kelly (1986), the river input for this region, comes from the rivers Sabine, Neches, Trinity, San Jacinto and San Bernard, as well as the Mississippi-Atchafalaya river system when there is downcoast circulation. In this region, May is the month with maximum freshwater, and October accounts for the minimum average river discharge. Therefore, it is expected to observe the shortest range in May and the longest range in October.

3) What is the oceanic circulation variability along the upper Texas coast for the period of June of 2016–November of 2017?

The temporal and spatial resolution of the HF radar provides information to describe the sub-mesoscale circulation variability and intensity, as well as observe the time when the direction reversal of the oceanic currents occurs. It is expected to observe the occurrence of a reversal on the circulation in June (from downcoast to upcoast) and

an increase in the power density between the 2–10 days, given that the weather band dominates over the inner shelf (Nowlin et al. 2005).

4) What are the dominant features of the circulation on the Texas coast?

Diurnal sea-breeze with 24-hour period and inertial oscillations with periods between 24.36–25.31 s^{-1} for the study area, generate an ocean basin with a near-resonant response to the wind stress, resulting in currents of up to 60 cm/s (DiMarco et al. 2000; Zhang et al. 2009).

Tidal varies spatially and temporally. The principal tidal constituents along LATEX are K1, O1, and M2, where the semidiurnal tides (M2) are amplified further offshore, with eastward cyclonic propagation, while the diurnal tides are in phase across and along the shelf (DiMarco and Reid 1998). Based on previous research on the LATEX shelf, the amplitude of the oscillations close to the coast (Chen et al. 1996)

1.4 Outline

The thesis is organized in five sections. Section 1 provided the introduction of the general circulation of the Gulf of Mexico, the motivation for this research and the research questions.

Section 2 describes the data and methods used to resolve the questions that drive the research. Section 3 consolidates the results obtained. Section 4 discusses how the results observed compare to previous observations on the variability of the circulation along the Texas coast and determines how the HF radar and buoy data compare.

Finally, Section 5 provides the conclusions and some recommendations for future research direction.

US Coast Guard (USCG) search and rescue (SAR) operations, oil spill monitoring,

2. DATA AND METHODS

2.1 Data

2.1.1 Texas Automated Buoy System (TABS)

TABS is operated and maintained by GERG and funded by the TGLO. Since 1996, TABS has provided near-real time atmospheric and oceanographic data for response and preparedness of the Texas coast. TABS consists of eight buoys (R, B, F, W, D, X, J, and K) equipped with sensors to measure oceanic currents, temperature, conductivity, and wind velocity (Guinasso et al. 2001; Walpert et al. 2011), as well as a communications link, a solar-powered electrical system, and the buoy flotation structure (Bender, Guinasso et al. 2007). There are two additional buoys funded by a consortium of industry partners at the Flower Garden Banks National Marine Sanctuary.

A Doppler Current Sensor (DCS) AANDERAA 4100/4100R installed in the buoys collects near surface ocean currents every 30 minutes. The DCS is located approximately 1.8 m below the surface (Bender et al. 2007), and operates at a frequency of 2MHz, offering an absolute speed accuracy of ±0.15 cm/s and a relative speed accuracy of ±1% of the reading. The current direction accuracy ranges from ±5º to ±7.5º for a 0–15º tilt to a 15–35º tilt, respectively. The DCS 4100 can operate between –10 to 50ºC with a depth capability of up to 300 m and a speed range of 0–300 cm/s (http://www.aanderaa.com/media/pdfs/dcs–4100–4100r.pdf).

Figure 5 illustrates the location of the TABS buoys and instantaneous wind and current information corresponding to January 30th of 2018, at 14:36:17 UTC.

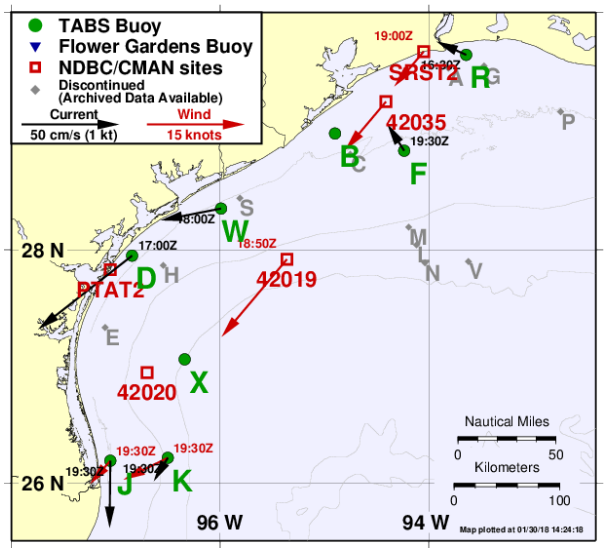

Figure 5. Map of the distribution of the TABS buoys (green) and the Flower Garden Bank's buoys (gray). The arrows denote speed and direction of oceanic currents (black) and winds (red), and represent the average for the last three hours of the data available up to 01/30/18 at 14:24:18. Bathymetric contours shown for these depths (meters): 20, 50, 200, 2000, 3500. Reprinted from http://tabs.gerg.tamu.edu.

2.1.2 High-Frequency Radar (HF Radar)

The experiments conducted by Heinrich Hertz based on James Clerk Maxwell's electromagnetic theories established the fundamentals of Radio Detection and Ranging (RADAR) systems in the late 1880s. However, it was not until the 1930s that radio waves were used for military purposes during World War II. In present days, radars have a wide variety of applications (Jensen 2007). In oceanography, HF radars emit frequencies between 3–30MHz, equivalent to wavelengths of 10–100m (Teague et al. 1997). This thesis focuses on ground wave radars to measure oceanic surface currents, although there are other transmission paths including the over-the-horizon radar, which operates using sky-wave transmission and reflect off the ionosphere (Paduan and Graber 1997).

The operation mechanism of the HF radar is based on an initial frequency pulse emitted by the transmitting antenna. Once the initial pulse reaches the roughness of the ocean surface, it reflects (backscatters) a frequency pulse to the receiving antenna as radials (polar beams) surrounding the system. The HF radar relies on the resonant backscatter of vertically polarized HF radio waves known as *Bragg scattering,* which results from the reflection from waves whose wavelength (λ) is half as long as that of the incident energy ($L = \frac{\lambda}{2}$), as sketched on Figure 6 (Barrick 1972; Howden et al. 2011; Paduan and Graber 1997) that are moving toward or away from the system. Using the first-order effect from the Bragg-scattering of surface gravity waves allows the quantification of 2-D ocean surface currents up to a 360º coverage. The second-order effect from the Bragg-scattering gives information about the waves (Paduan and Graber 1997; Teague et al. 1997).

The frequency backscattered will depend on the Doppler effect. The Doppler shift due to the Bragg waves is known, hence, any additional Doppler shift is attributed to the underlying ocean currents (Figure 7) (Paduan and Graber 1997). The shift of the spectral peak, is given by $\Delta f = \frac{2v_{cr}}{\lambda}$, where v_{cr} is the mean effective radial velocity (Barrick et al. 1977).

Due to the principle of operation of the HF radar, propagation of the signal is dependent upon the conductivity of the water (Figure 8). The salts dissolved in the seawater enhance the propagation of the electromagnetic pulse, therefore, the HF radar does not perform well in freshwater (Gurgel et al. 1999).

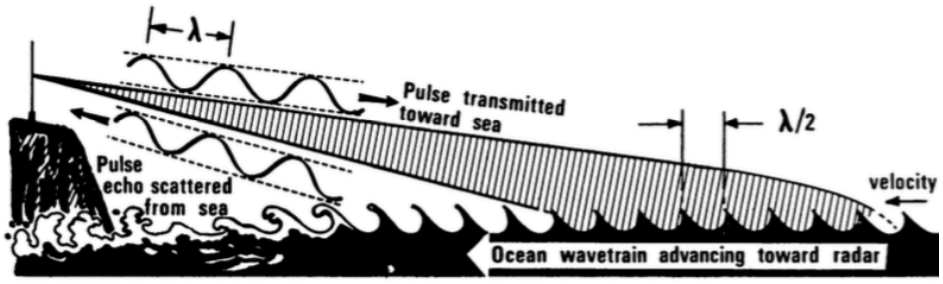

Figure 6. The diagram represents a radar antenna emitting an electromagnetic signal with a wavelength $\boldsymbol{\lambda}$, which receives an echo pulse backscatter of a $\boldsymbol{\lambda/2}$ wavelength, based on the Bragg scatter principle. Reprinted from Barrick et al. (1977).

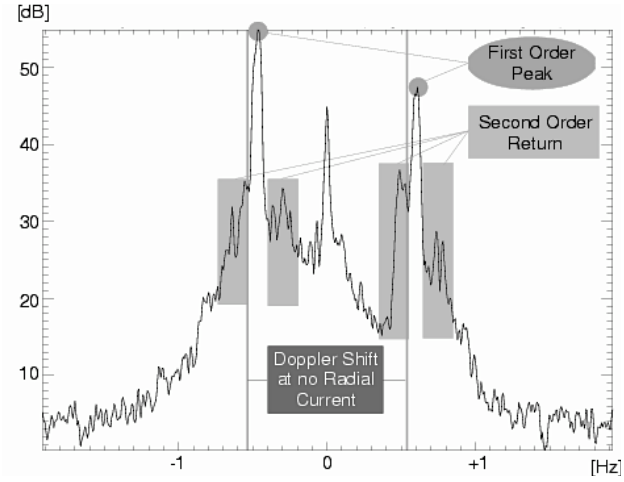

Figure 7. The HF radar spectrum sketched on this figure represents the first and second order Bragg scattering, with an offset on the first order peak due to underlying currents. The gray lines represent the zero Doppler shift frequency. Reprinted from https://marine.rutgers.edu/cool/education/spring2000/kristiea/project1.html.

Each HF radar site consists of a transmitter antenna, a receiver and a trailer to store the electronics, separated one λ. The range, penetration depth, resolution, and bandwidth of the HF-radar will depend on the wavelength emitted. Common frequencies are listed in **Table 1**, as well as their corresponding radar and ocean wavelength, i.e., λ

and λ/2, as well as the expected range, penetration depth and typical resolutions. The HF radar installed on the Texas coast is a long-range system that operates at a frequency of 4.45 MHz with an expected range of 180 km offshore with a spatial resolution of 6 km, a temporal resolution of one hour, and accuracy of 2–4 cm/s.

A single radar antenna measures only the flow along a radial beam emanating from the site. To estimate total surface velocities, it is necessary to combine at least two radials with an angle >30° and <150° (Paduan and Graber 1997). The receiver-transmitter pair has to be located within a distance of 40–60% of the radar's offshore range. Figure 9 represents two sites resolving the total velocity at a specific location by using the radials obtained from each site within a specific grid spacing.

First, the orthogonal components *u* (zonal) and *v* (meridional) are resolved for all vectors within each grid where the intersection between site 1 and site 2 occurs. The angles of the radials are given by θ_1 and θ_2, respectively. Then, the least squares from *u* and *v* are combined to estimate the total velocity vector. Lastly, *u* and *v* are combined to generate a total vector. The total vector is given by the intersection of the orthogonal planes of *u* and *v* as shown in Figure 10 (http://codar.com). Note that for this thesis the estimation of total vectors from radials was not performed, the totals were downloaded from the Coastal Observing Research and Development Center (*http://hfrnet–tds.ucsd.edu/thredds/catalog.html*).

For the Texas coast, the radar sites are listed below and shown in Figure 11 with an example of their output:

RLVR: Rollover Pass *(installed as of January of 2018)*
SSDE: Surfside Beach *(installed as of January of 2018)*
MBNP: Matagorda Bay Nature Park

ANWR: Aransas National Wildlife Refuge

PINS: Padre Island Nature Seashore *(installed as of January of 2018)*

PMPI: Port Mansfield Padre Island

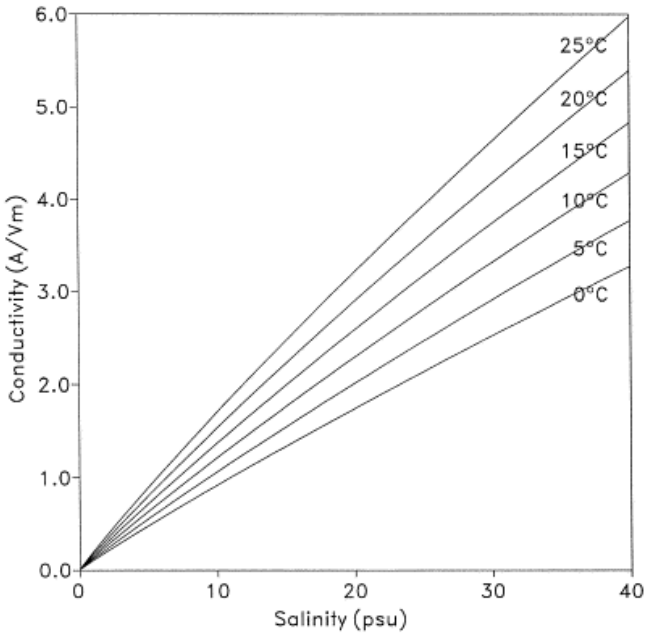

Figure 8. Conductivity of seawater as a function of salinity for six different temperatures. Reprinted from Grugel et al. (1999).

Table 1. HF radar parameters for different emitted frequencies. Reprinted and adapted from http://codar.com.

Frequency (MHz)	Radar Wavelength λ (m)	Ocean Wavelength λ/2 (m)	Range (km)	Depth of Current (m)	Typical Resolution (km)
5	60	30	140–220	2	6–12
13	23	11.5	45–75	1–1.5	2–5
25	12	6	30–40	.5–1	1–3
42	7	3.6	15–20	<. 5	0–25–1

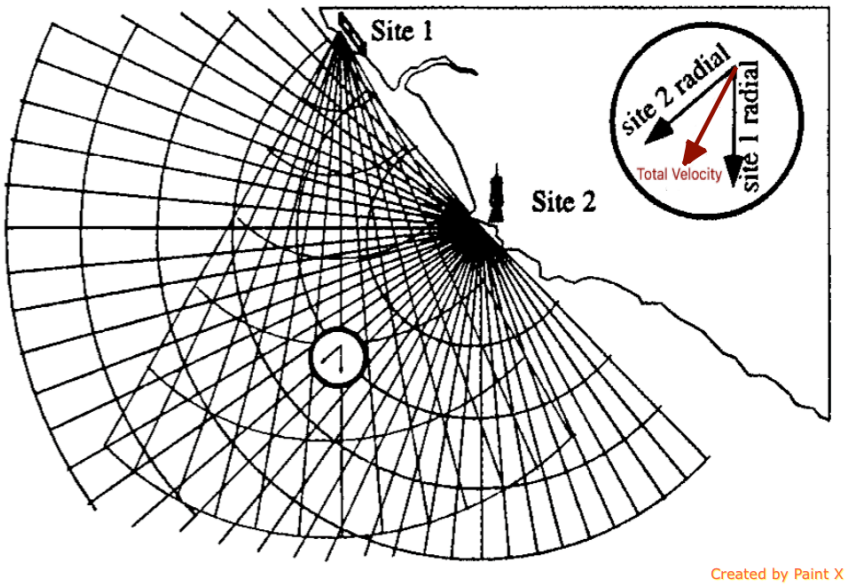

Figure 9. The illustration sketches two sites emitting their radial components. A zoom of the intersection (circle at the top right corner) shows the total velocity estimated with these radials (maroon vector). Reprinted and adapted from Paduan and Graber (1997).

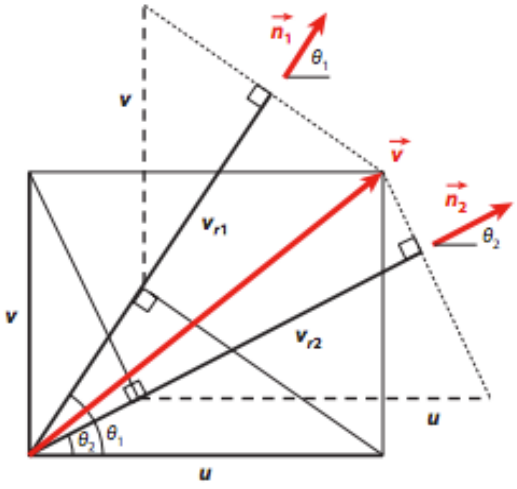

Figure 10. The diagram is a geometric representation of the total velocity solution. θ1 and θ2 are the angles of the radials for site 1 and site 2, respectively. The dotted lines represent the orthogonal planes to the *u* (zonal) and *v* (meridional) radial components, where V is the resulting velocity. Reprinted and adapted from http://ambipetro.com.br.

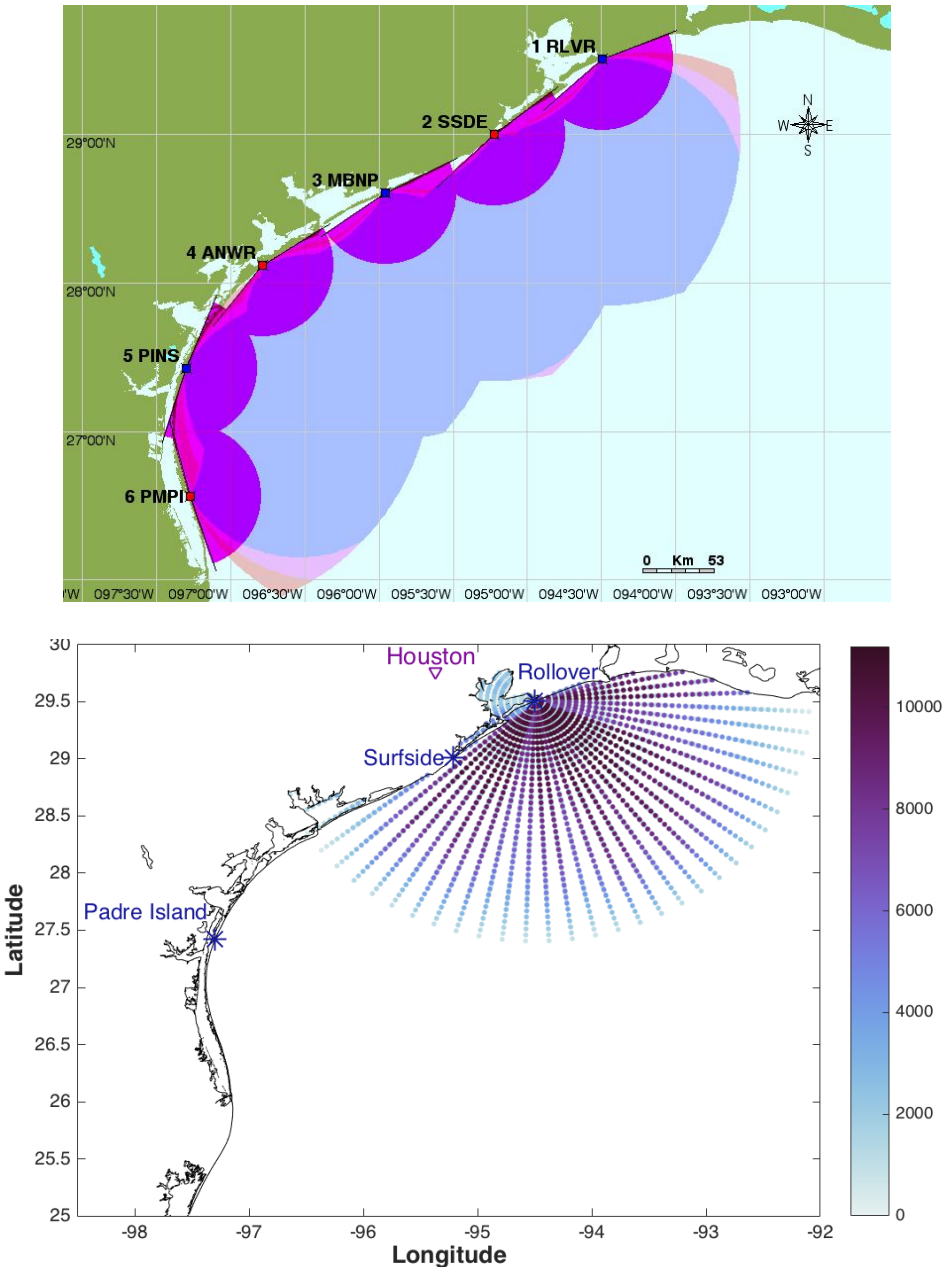

Figure 11. (Top) The map shows the location of the HF radar sites (blue and red squares) and the expected observational coverage for the Texas coast. The magenta semi-circles indicate the bearing limits. The blue, pink and orange shades represent the 30º, 25º, and 20º stability angles, respectively. Map created using CODAR's SeaDisplaySetup software by Dr. Kerri Whilden (TAMU/GERG). (Bottom) Radials output from Rollover (RLVR), where the dark colors represent more data collected, and the light blue represent few measurements collected.

2.2 Methods

The datasets for this thesis consist of the time series from June 9th of 2016–November 30th of 2017, of the TABS buoys W, R, F, B, the radials from the HF radar, and the estimated totals from those radials. The outputs from the TABS buoys, RLVR, and SSDE are a zonal (E-W) and a meridional (N-S) component for each system. The zonal and meridional component of RLVR and SSDE contribute to form a total velocity vector throughout the HF radar footprint as explained in the previous section, which can be decomposed in a zonal and meridional component (Figure 12). The former zonal and meridional are a joint contribution of both radar systems. Figure 13 shows a composite of the data collected by the HF radar and the TABS buoys, where each season is defined as:

- Winter: December–February
- Spring: March–May
- Summer: June–August
- Fall: September–November

Seasons (summer–2016/summer–2017 and fall–2016/fall–2017) are analyzed separately anticipating that the HF radar operations were under different constraints on each season such as technical problems (calibration, power issues, outside noise) and the impact of Harvey (August–September, 2017). For the summer of 2017 data gaps account for 19% of the dataset, i.e., 18 days without data, and for the fall of 2017 data gaps add up to 28% of the data, i.e., 26 days. Given the temporal separation within the data available, a linear interpolation was not preformed for the last 200 points of summer 2017 (6.5 days of data) nor the first 760 hours of the fall 2017 (31 days of data), and these points were removed of the record instead.

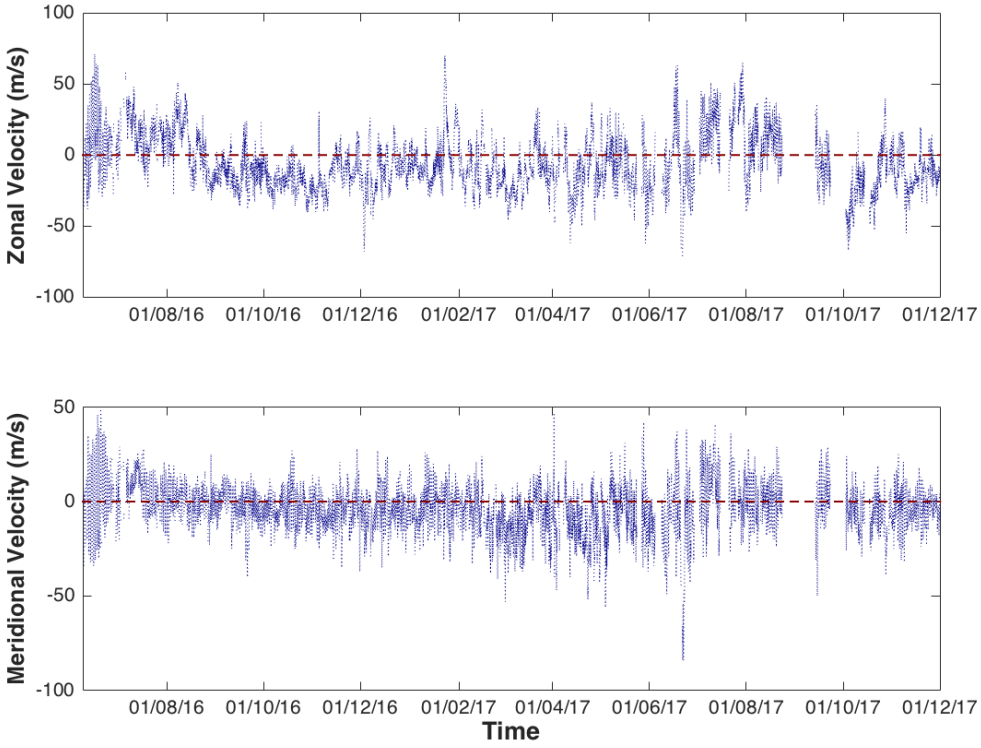

Figure 12. Time series of zonal (top) and meridional (bottom) components of the HF radar from June 9th, 2016 to November 30th, 2017. The red dotted line is a reference line located at zero m/s.

For the operating frequency of the HF radar system on the Texas coast (4.45 MHz), the receiver-transmitter pair has to be located within a distance of 40-60% the expected range (72–108 km for a 180 km expected range). The distance between RLVR and SSDE is 88.9 km and the distance between SSDE and PINS is 269.6 km. Given that the distance between SSDE and PINS is twice the maximum ideal, the resulting vectors from the pair SSDE-PINS are neglected in this thesis. To neglect the data from PINS and remove noise on the edges of the HF radar footprint constructed with the combined

output from RLVR and SSDE, a manually traced contour is used to keep only those data points contained within a narrower range (Figure 14).

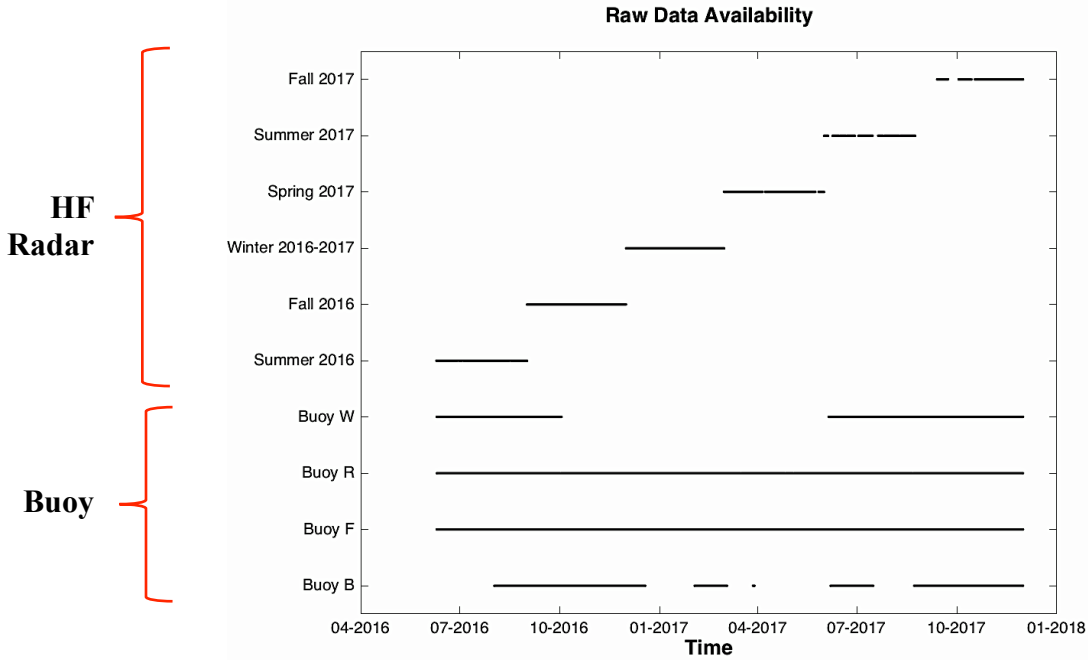

Figure 13. Composite of data availability for the HF radar and each TABS buoy used in this thesis.

The minimum distance offshore perpendicular to the coastline, considered in this thesis and corresponding to the midpoint between RLVR and SSDE, is 10 km, and the maximum is 129.6 km (close to the 50m isobath). The minimum and maximum range (distance offshore from the instrument, an indicator of how far the instruments could capture a measurement) are 6.7 km and 144.6 km for RLVR, and 12.38 km and 147.5 km for SSDE.

The data analysis consists of a comparison of TABS and HF radar, estimation of the data collected by the HF radar per season, calculation of variance ellipses within the HF radar footprint, spectral analysis (power spectra and rotary spectra), wavelet analysis,

tidal analysis, and coherence. For wavelet, power spectra, rotary spectra, and coherence, the data is rotated by 38.7º to obtain the alongshore and cross-shore component, instead of the zonal (E-W) and meridional (N-S) component.

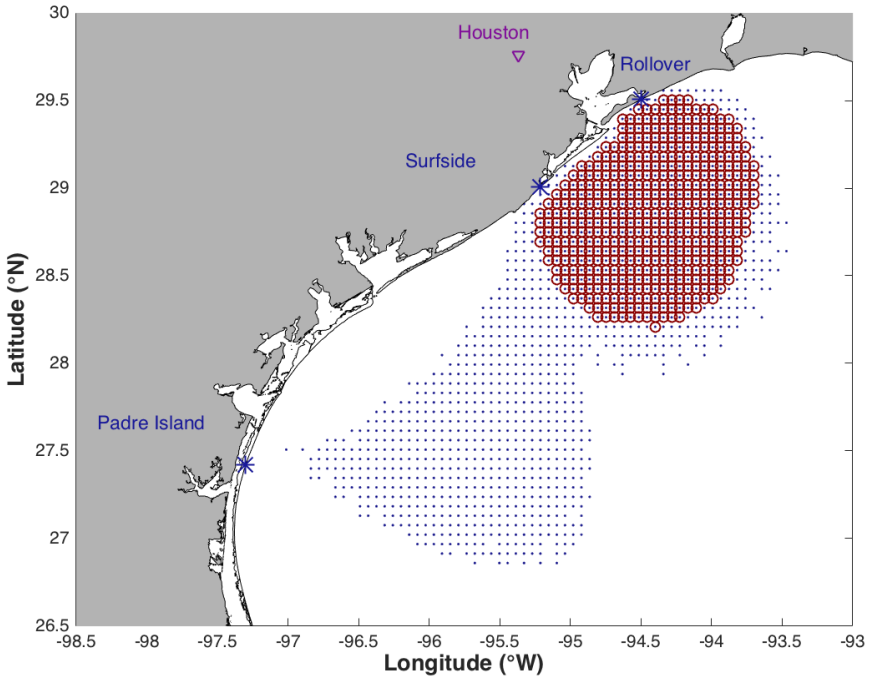

Figure 14. Original (blue) and trimmed (red) HF radar grid footprint. Each dot represents a bin of data collected thought the time series.

2.2.1 Vector Projection of Buoy Data along Radials

To compare the current measurements from TABS and HF radar using the same reference system, the buoy data was projected along the closest HF radar radial and both time series (buoy and HF radar) were linearly interpolated to have equally spaced data

time stamps. The next equation provides the projection of the buoy vector (*b*) onto the radar radial vector (*r*), where the numerator is the dot product of *r* and *b*:

$$proj_r b = \frac{\vec{r} \cdot \vec{b}}{\vec{r} \cdot \vec{r}} \vec{r} = \frac{\vec{r} \cdot \vec{b}}{|\vec{r}|^2} \vec{r}$$

The output of each site of the radar and each buoy is a zonal (E-W) and a meridional (N-S) component. Therefore, for each radar-buoy comparison, it is possible to compare the zonal (meridional) component of the radar with the projected zonal (meridional) component of the buoy.

For each comparison, basic statistical parameters are provided (minimum, maximum and mean), histograms to compare the frequency distribution of both measurement systems, and correlation coefficients.

Mean:

The sample mean for a sample with *N* elements, is calculated as:

$$\bar{x} = \frac{1}{N} \sum_{i=1}^{N} x_i$$

Frequency of occurrence diagram:

The histogram summarizes how often a value occurred within a data set. In this particular case, the histograms summarize how often the measurements are contained within a range of velocities.

Correlation coefficient:

Correlation determines how well two or more variables co-vary. For this thesis, a correlation coefficient is obtained for each comparison, i.e., zonal (meridional) RLVR vs. projected zonal (meridional) of Buoy F (W, R, and B). For two variables (*x* and *y)* of length N, the correlation coefficient *R (-1≤R≤1*) is given by:

$$R = \frac{1}{N-1}\sum_{i=1}^{N}\frac{(x_i - \bar{x})(y_i - \bar{y})}{s_x s_y}$$

$$R = \frac{C_{xy}}{s_x s_y}$$

Where C_{xy} is the covariance of *x* and *y,* and s_x and s_y are the corresponding standard deviations:

$$C_{xy} = \frac{1}{N-1}\sum_{i=1}^{N}(x_i - \bar{x})(y_i - \bar{y})$$

A perfect correlation is given by *R=-1* (180º out-of-phase) or *R=1* (in-phase). When $r \approx 0$, means there is little to no correlation between the variables.

The squared value of the correlation coefficient, R^2 ($0 \leq R^2 \leq 1$), is the ratio of variance explained (SSR) to total variance (SST). R^2 measures the value that a linear regression of y on x explains the total sample variance:

$$R^2 = \frac{{C_{xy}}^2}{(s_x s_y)^2} = \frac{SSR}{SST}$$

2.2.2 Seasonality of Data Availability

To estimate percent of data availability per season, the sum of the number of measurements collected per bin (defined as a 6 km grid where a total vector is estimated from the radials) was estimated and normalized by the maximum number of days in the season. The cell with maximum data available per season is used on the wavelet, spectral and coherency analysis

2.2.3 Variance Ellipses Basic Statistics

Variance:

For a time series x with mean value $\bar{x}$, the sample variance can be estimated as:

$$s^2 = \frac{1}{N-1}\sum_{n=1}^{N} = (x_n - \bar{x})^2$$

The standard deviation, $s = \sqrt{s^2}$, measures how the data are spread around the mean. On a normal distribution, 95% of the measurements are contained within ± 2 standard deviations.

Variance ellipses represent the isotropy or anisotropy of the variability, as well as the direction where the most of the variability is occurring. The zonal and meridional components from the HF radar were used to estimate the variance ellipses. The semi-minor (*m*), semi-major (*M*) axis, and the angle of the variance ellipses (θ) are given by (Thomson and Emery 2014):

$$\frac{M}{m} = \frac{1}{2}\left\{\left(\overline{u^2} + \overline{v^2}\right) \pm \left[\left(\overline{u^2} + \overline{v^2}\right)^2 + 4(\overline{uv})^2\right]^{1/2}\right\}$$

$$\theta = \frac{1}{2}\tan^{-1}\left[\frac{2\overline{uv}}{\overline{u^2} - \overline{v^2}}\right]$$

Where $\overline{u^2}$ is the squared mean of the zonal component (E-W) and $\overline{v^2}$ is the squared mean of the meridional (N-S) component.

2.2.4 Power Spectra

A frequency spectrum of a time-domain signal is an equivalent representation of that signal in the frequency domain. Spectral analysis of the alongshore and cross-shore component of the HF radar is useful to partition the variance of a time series as a function of frequency, where the contributions from the different frequency components are measured in terms of the power spectral density (PSD).

For a discrete time series $y(t_n) = y_n$ with time sampling interval Δt, and finite time duration $T = N\Delta t$, where $n = 1\ to\ N$. The energy spectral density is the absolute value of the squared Fourier transform of the continuous representation of the discrete time series, and is called a periodogram (Thomson and Emery 2014).

Continuous representation:

$$y_s(t) = y(t) \sum_{n=1}^{N} \delta(t - n\Delta t)$$

Fourier transform:

$$Y_k(f) = \Delta t \sum_{n=1}^{N} y_n \, e^{-i2\pi f_k n \Delta t}$$

$$Y_k(f) = \Delta t \sum_{n=1}^{N} y_n \, e^{-i2\pi kn/N}; \qquad f_k = \frac{k}{N\Delta t}, k = 0, \dots, N$$

The frequencies f_k are confined in the Nyquist frequency:

$$f_N = \frac{1}{2\Delta t} \; ; \begin{cases} 0 \le f_k \le f_N \; ; & k = 0, \dots, N/2 \\ -f_N \le f_k \le 0 \; ; & k = N/2, \dots, N \end{cases}$$

Energy spectral density:

$$S_E(f) = |Y_k|^2 \; ; \; k = 0, \dots, N-1$$

Parseval's energy conservation:

$$\Delta t \sum_{n=1}^{N} |y_n|^2 = \Delta f \sum_{k=0}^{N-1} |Y_k|^2 \; ; \qquad \Delta f = \frac{1}{N\Delta t}$$

For this thesis, the time series are the alongshore and cross-shore components, and the sampling interval is 1/24 hrs.

The Welch's Method is used to smooth the alongshore and cross-shore power spectra. This method involves sectioning the record (Welch 1967). The alongshore and

cross-shore time series are sub-sampled using a 256-point Kaiser-Bessel window with an overlap of 50%. The Kaiser-Bessel window treats statistically independent every 256-point segment, increasing the degrees of freedom and, therefore, the statistical confidence of each spectra estimate.

The raw power spectral density is plotted, with the Kaiser-Bessel smoothed data bounded by a 95% upper and lower confidence interval. A 40-hr low-pass filter was applied to remove the tidal and inertial oscillations. And based on the Kolmogorov -5/3 law (Cushman-Roisin and Beckers 2011), a -5/3 reference line was added, to compare the theoretical cascade with the cascade of the low frequencies in the dataset of this thesis.

2.2.6 Tidal Analysis

The changing alignment of the sun, moon and earth, generates changes in the gravity field of the moon and sun over the earth; this gradient of the gravity field is the driving force of tides. The tidal constituents have general symbols M (moon) for lunar origin and S (sun) for solar origin, and the subscripts 1 and 2 refer to diurnal and semidiurnal oscillations, ~24-hour period and ~12-hour period, respectively. The major diurnal and semidiurnal tidal constituents are shown in **Table 2** (DiMarco 1998; Kowalik and Luick 2013).

This thesis analyzes the first eight tidal constituents (O1, K1, P1, Q1, S2, M2, K2, and N2) of the alongshore and cross-shore velocity components using the method of cyclic descent (MCD) to estimate amplitude and phases of the tides. Tidal ellipses for each tidal constituent are built from the zonal and meridional components from the HF

radar for each season, and the principal tidal constituents are estimated using the full record and the record with the summers removed, in agreement to DiMarco (1998).

Table 2. Major diurnal and semidiurnal tidal constituents. Adapted from (DiMarco 1998; Kowalik and Luick 2013).

Constituent	Name	Period (Mean solar hour)
Semidiurnal		
M2	Principal lunar	12.42060
S2	Principal solar	12.00000
N2	Larger lunar elliptic	12.65835
K2	Luni-solar declination	11.96724
Diurnal		
K1	Luni-solar declination	23.93447
O1	Principal lunar	25.81934
P1	Principal solar	24.06589
Q1	Larger lunar elliptic	26.86836

The method of cyclic descent (MCD), originally described by Bloomfield (1976), is based on iterated least squares to fit a model equation to data time series, and optimizes the phase and frequency of the dataset even if this contains gaps (DiMarco 1998). The MCD allows constructing tidal ellipses from the phase and amplitudes of the east-west (u) and north-south (v) components of each tidal constituent, describing the maximum kinetic energy in the study area. The major (M) and minor (m) axes of the tidal ellipses are defined as (Godin 1972):

$$\frac{M}{m} = \frac{1}{2}[\sqrt{(a_u + b_v)^2 + (a_v - b_u)^2}] \pm \sqrt{(a_u - b_v)^2 + (a_v + b_u)^2}$$

Angle of M relative to the east-west axis:

$$\alpha = \frac{1}{2}(\alpha_1 + \alpha_2)$$

Where $\alpha_1$and α_2 are defined by:

$$\alpha_1 = \tan^{-1}\frac{(a_v - b_u)}{(a_u + b_v)}$$

$$\alpha_2 = \tan^{-1}\frac{(a_v + b_u)}{(a_u - b_v)}$$

2.2.5 Rotary Spectra

The Rotary spectra resolve an ocean surface velocity vector into clockwise and counterclockwise components (clockwise rotation of the wave vector corresponds to an eastward phase propagation with time) (Hayashi 1979). On this thesis, Rotary spectra are calculated using the alongshore and cross-shore components of surface currents, instead of zonal and meridional components as described below.

The rotary spectra isolate inertial currents, which have a characteristic clockwise rotation in the northern hemisphere (Saji et al. 2000), from a tidal signal, which typically has both clockwise and counterclockwise components (Gonella 1972). For example, in the West Florida Shelf, the diurnal and semidiurnal spectral peaks are well resolved in the clockwise rotary spectra (Liu et al. 2014) while in the Atlantic Ocean (39º N) diurnal tides are better defined in the counterclockwise spectrum (Gonella 1972). In general, the motions are predominantly clockwise in the northern hemisphere (Thomson and Emery 2014).

A horizontal velocity can be defined as a complex function in a Cartesian coordinates, with real u (eastward) component and imaginary v (northward) component,

where $w=u+iv$ (Mooers 1973; Thomson and Emery 2014). The angular frequency, σ, is always positive and the angular velocity ω is positive ($\omega = +\sigma$) for counterclockwise rotation or negative for clockwise rotation. The coefficients of the Fourier transform of the complex time series w computed from the sine and cosine Fourier coefficients of u and v for $\sigma = |\omega|$ are:

$$u_\sigma = a_1 \cos(\sigma t) + b_1 \sin(\sigma t)$$

$$v_\sigma = a_2 \cos(\sigma t) + b_2 \sin(\sigma t)$$

Where:

$$w_\sigma = a_1 \cos(\sigma t) + b_1 \sin(\sigma t) + i\,[a_2 \cos(\sigma t) + b_2 \sin(\sigma t)]$$

With the auto-spectra of u and v (P_{uu} and P_{vv}), the cross-spectra (P_{uv}) and the quadrature spectra (Q_{uv}) it is possible to estimate the clockwise and counterclockwise spectrum (Gonella 1972):

$$P_{uu} = \langle {a_1}^2 + {b_1}^2 \rangle$$

$$P_{vv} = \langle {a_2}^2 + {b_2}^2 \rangle$$

$$P_{uv} = \langle a_1 a_2 + b_1 b_2 \rangle$$

$$Q_{uv} = \langle a_1 b_2 - a_2 b_1 \rangle$$

Clockwise spectrum:

$$S_- = \frac{1}{8}(P_{uu} + P_{vv} - 2Q_{uv})$$

Anticlockwise spectrum:

$$S_+ = \frac{1}{8}(P_{uu} + P_{vv} + 2Q_{uv})$$

2.2.6 Wavelet Analysis

For this thesis, wavelet analysis will be performed to provide the frequency evolution of the spectral energy distribution throughout the length of the time series (~17.5 months of data) for the alongshore component of the HF radar for the raw and detided record. Variations in power allow the identification of oceanographic features based on the energetic frequency bands and dominant modes of variability with time (Thomson and Emery 2014; Torrence and Compo 1998). Subtracting the mean and dividing by the standard deviation, standardize the time series.

The wavelet analysis is performed using a scaled (wavelet scale s) and translated (along the time index n) Morlet wavelet (nonorthogonal wavelet function, $\varphi_0(\eta)$, with normalized complex conjugate φ^*, for a continuous wavelet transform of a discrete time series (x_n) with time step δt and N number of points), consisting of a plane wave modulated by a Gaussian envelope of unit width, and defined as a convolution of x_n (Torrence and Compo 1998):

$$W_n(s) = \sum_{n'=0}^{N-1} x_{n'}\, \varphi^* \left[\frac{(n'-n)\delta t}{s}\right]$$

Using a discrete Fourier transform (DFT), the wavelet transform is defined as the inverse Fourier transform of:

$$W_n(s) = \sum_{n'=0}^{N-1} \hat{x}_k\, \hat{\varphi}^*(s\omega_k) e^{i\omega_k n \delta t}$$

Where the Fourier transform of $\varphi(t/s)$ is $\hat{\varphi}(s\omega)$, $k = 0 \ldots N-1$ and the DFT of x_n is:

$$\hat{x}_k = \frac{1}{N} \sum_{n=0}^{N-1} x_n e^{-2\pi i k n/N}$$

And the angular frequency ω_k is defined as:

$$\omega_k = \frac{2\pi k}{N\delta t} : \; k \leq \frac{N}{2}; \; -\frac{2\pi k}{N\delta t} : \; k > \frac{N}{2}$$

A normalized wavelet function guarantees that the amplitude of the Fourier coefficients ($\hat{x}_k$) weights the wavelet transform. From the last equations we can define:

Amplitude:

$$|W_n(s)|$$

Phase ($\Im: Imaginary; \; \Re: Real$):

$$\tan^{-1} \frac{\Im\{W_n(s)\}}{\Re\{W_n(s)\}}$$

Wavelet power spectrum:

$$|W_n(s)|^2$$

The computing of the wavelet analysis is performed using the software available at *http://paos.colorado.edu/research/wavelets/software.html* created by Torrence and Compo. The Torrence and Compo software allows the user to change the parameters that will define the wavelet transform, returning the cone of influence ($\sqrt{2}s$ for a Morlet wavelet) and the 95% confidence contour found through a chi-squared distribution. The authors suggest that the set of scales is a fractional power of two:

$$s_j = s_0 2^{j\delta j}, j \; = 0,1, \ldots, J$$

$$J = \delta j^{-1} log_2(N\delta t / s_0)$$

Where s_0 is the smallest resolvable scale (approximately $2\delta t$), J determines the largest scale, and the largest recommended sampling in scale (δj) for the Morlet wavelet is 0.5. In order to limit the edge effects, the time series can be padded with zeroes to bring N to the next power of two. Liu et al. (2007) demonstrated that the wavelet method of Torrence and Compo does not

produce a spectrum with identical peaks for a time series comprised of sine waves with the same amplitude at different frequencies. As a result of this bias, peaks in the spectrum get smoothed out at small scales, while at large scales the peaks are sharper and have larger amplitude. Liu et al. (2007) propose a bias rectification, which consists of dividing the wavelet power spectrum by its scales. This rectification results in an improvement in the spectral estimate (Liu et al. 2007).

2.2.7 Coherence Analysis

The coherence-squared function allows to determine the correlation between the alongshore and cross-shore component of the current velocity measured with HF radar, for each season captured throughout the length of the time series. To remove variance from the record, the mean of each season is subtracted.

The coherence-squared function quantifies the correlation in frequency ($f_k, k = 0,1,\dots,N-1$) of two individual observations (x, y), and is defined as (Thomson and Emery 2014):

$$\gamma_{xy}{}^2(f_k) = \frac{\left|P_{xy}(f_k)\right|^2}{P_{xx}(f_k)P_{yy}(f_k)} \; ; \; f_k > 0$$

$$\gamma_{xy}(f_k) = \left|\gamma_{xy}{}^2(f_k)\right|^{1/2} e^{-i\phi_{xy}f_k}$$

$$0 \leq \left|\gamma_{xy}{}^2(f_k)\right| \leq 1$$

Two signals that are being compared are considered highly coherent and in phase when $\left|\gamma_{xy}{}^2(f_k)\right| \approx 1$ and the phase lag $\phi_{xy}(f_k) \approx 0$.

The confidence interval is helpful to set the limiting value up to which coherence-square values can occur. Common confidence intervals are α=0.10 (90%), α=0.05 (95%) and α=0.01

(99%). The significance level for the coherence-square is given by (Thompson 1979; Thomson and Emery 2014):

$$\gamma^2{}_{1-\alpha} = 1 - \alpha^{1/(EDOF-1)}$$

$$\gamma^2{}_{1-\alpha} = 1 - \alpha^{2/(DOF-2)}$$

Where the equivalent degrees of freedom, EDOF=DOF/2, is the number of independent cross-spectral realizations in each frequency band.

3. RESULTS

3.1 Vector Projection of Buoy Data along Radials

The total velocity estimated from the radials is a contribution of two (or more) radials measuring the speed of the same area. Each radial has a different bearing angle, and therefore, a different contribution to the estimation of the total velocity. The difference in bearing angles leads to a difference in the projection of the buoy data along each radial, i.e., the projection of the zonal component of buoy B along the closest radial from RLVR is different to the projection of the same component along the closest radial from SSDE. Note the case of buoy F, summer 2017, depicted in Figure 15; in this case, RLVR and SSDE are located on opposite directions from buoy F, similar bearing angles in magnitude, with opposite direction. The result of this geometric arrangement is that the magnitude of the projection of the zonal component along the SSDE radial resembles that of the projection of the meridional component along the RLVR radial, and vice versa. Therefore, the correlation coefficient between the radial and projected buoy only makes reference to the relationship between both measurement systems but this correlation does not characterize the circulation on the Texas shelf. Instead, the total vectors are the metrics that provide information about the measured velocity ranges of the zonal, meridional, alongshore or cross-shore components on this region. Note the similarity of the probability distributions on Figure 15, in both panels, the HF radar system showed more spreading than TABS.

Due to the incidence angle, the projected zonal component of RLVR resembles the projected meridional component of SSDE. When comparing radial data against buoy projection

along radials, buoy F proved to have the greatest correlation coefficients. The latter is due to the fact the buoy F is centrally located within the HF radar data cloud coverage.

Five out of six seasons recorded their greatest correlation coefficient when comparing SSDE HF radar radial data with buoy F, with ten seasons having a correlation coefficient above 0.5, while RLVR only had three seasons exceeding this number. When comparing RLVR to buoy F data, summer 2016 had the greatest correlation coefficient (0.75).

Overall, winter had the greatest correlation coefficient of all the seasons (0.87), spring had the second largest (0.79), closely followed by summer 2016 (0.75), then summer 2017 (0.66), fall 2017 (0.59) and lastly fall 2016 (0.47). This section summarizes the comparison of the minimum, maximum, mean, and standard deviation of the RLVR and SSDE radial data nearest to the location buoy B, F, R or W, against the vector projection of the buoy data along the latter radial. Table 3 and Table 4 summarize the metrics (minimum maximum and mean value) for RLVR radials and the projection of the buoy data. The correlation coefficients (R) between the projected buoy data and the radial data are included, as well as the p-value. Only two decimals points are indicated, and since in the p-values were below 10^{-10}, they appear as zeroes.

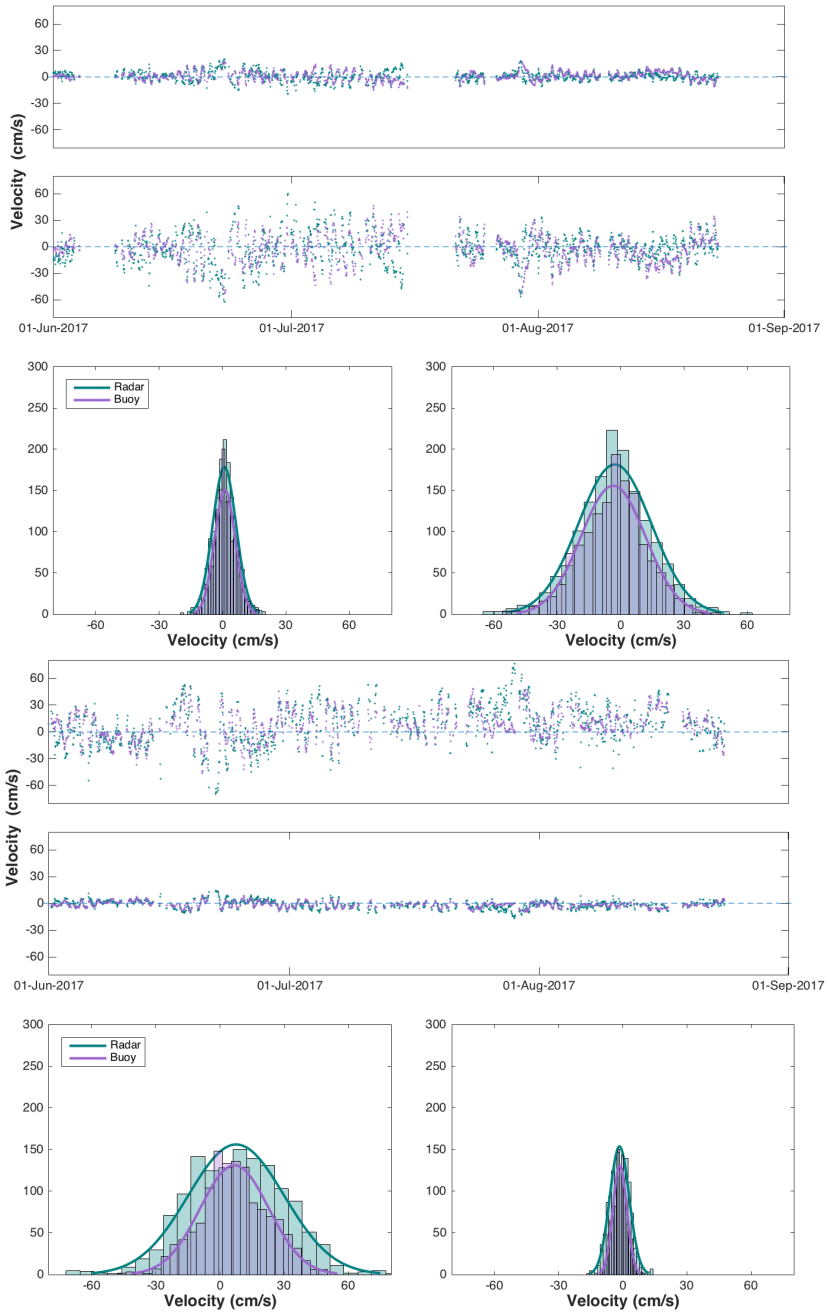

Figure 15. The top panel shows the time series of the zonal (top-top) and meridional (top-bottom) components of RLVR radial and the projected buoy along the radials, followed by the histogram for the zonal component (top-left) and meridional component (top-right). The bottom panel shows the same plots for SSDE. The HF radar radial is represented with turquoise) and the projection of buoy F with purple.

Table 3. Metrics for the zonal (u) and meridional (v) component of the RLVR radials and the projected buoy data in cm/s.

	RLVR Winter 2016-2017				RLVR Spring 2017				RLVR Summer 2016			
	Buoy B											
	Min	**Max**	**Mean**	**Std**	**Min**	**Max**	**Mean**	**Std**	**Min**	**Max**	**Mean**	**Std**
Radar u	-13.34	15.62	0.76	3.68	-12.74	16.91	2.41	4.46	-17.55	17.37	-0.01	6.66
Radar v	-48.42	41.34	-2.35	11.41	-52.40	39.48	-7.48	13.83	-53.82	54.38	0.02	20.63
Buoy u	-9.02	13.72	1.45	2.93	-5.29	12.45	3.21	4.17				
Buoy v	-42.49	27.95	-4.49	9.09	-38.57	16.39	-9.95	12.93				
	R^2 u	**P-value**	**R^2 v**	**P-value**	**R^2 u**	**P-value**	**R^2 v**	**P-value**				
	0.41	0.00	0.41	0.00	0.64	0.00	0.64	0.00				
	Buoy F											
	Min	**Max**	**Mean**	**Std**	**Min**	**Max**	**Mean**	**Std**	**Min**	**Max**	**Mean**	**Std**
Buoy u	-10.39	12.91	-0.43	2.40	-12.75	12.82	-0.39	3.34	-17.86	17.43	0.37	5.58
Buoy v	-40.02	32.21	1.32	7.45	-39.74	39.52	1.20	10.36	-54.02	55.36	-1.16	17.29
	R^2 u	**P-value**	**R^2 v**	**P-value**	**R^2 u**	**P-value**	**R^2 v**	**P-value**	**R^2 u**	**P-value**	**R^2 v**	**P-value**
	0.53	0.00	0.53	0.00	0.46	0.00	0.46	0.00	0.75	0.00	0.75	0.00
	Buoy R											
	Min	**Max**	**Mean**	**Std**	**Min**	**Max**	**Mean**	**Std**	**Min**	**Max**	**Mean**	**Std**
Buoy u	-14.97	14.35	-0.57	2.53	-15.19	11.95	-0.73	3.15	-6.70	10.16	0.49	1.98
Buoy v	-44.47	46.38	1.76	7.85	-37.12	47.07	2.28	9.76	-31.48	20.78	-1.51	6.13
	R^2 u	**P-value**	**R^2 v**	**P-value**	**R^2 u**	**P-value**	**R^2 v**	**P-value**	**R^2 u**	**P-value**	**R^2 v**	**P-value**
	0.19	0.00	0.19	0.00	0.21	0.00	0.21	0.00	0.23	0.00	0.23	0.00
	Buoy W											
									Min	**Max**	**Mean**	**Std**
Buoy u									-14.79	13.44	-2.25	4.77
Buoy v									-41.65	45.84	6.98	14.78
									R^2 u	**P-value**	**R^2 v**	**P-value**
									0.22	0.00	0.22	0.00

Table 3. Continued.

	RLVR Summer 2017				RLVR Fall 2016				RLVR Fall 2017			
	Buoy B											
	Min	**Max**	**Mean**	**Std**	**Min**	**Max**	**Mean**	**Std**	**Min**	**Max**	**Mean**	**Std**
Radar u	-19.31	20.11	0.86	5.56	-14.88	15.56	0.26	3.56	-9.32	15.27	1.69	3.32
Radar v	-62.32	59.84	-2.67	17.23	-48.22	46.12	-0.82	11.04	-47.31	28.88	-5.24	10.27
Buoy u	-17.02	13.68	-0.41	4.89	-9.18	11.68	1.52	3.14	-15.37	9.30	-1.90	3.68
Buoy v	-42.39	52.74	1.27	15.16	-36.19	28.44	-4.71	9.73	-28.94	47.57	5.89	11.41
	R^2 u	**P-value**	**R^2 v**	**P-value**	**R^2 u**	**P-value**	**R^2 v**	**P-value**	**R^2 u**	**P-value**	**R^2 v**	**P-value**
	0.32	0.00	0.32	0.00	0.22	0.00	0.22	0.00	-0.04	0.09	-0.04	0.09
	Buoy F											
	Min	**Max**	**Mean**	**Std**	**Min**	**Max**	**Mean**	**Std**	**Min**	**Max**	**Mean**	**Std**
Buoy u	-14.84	17.14	1.12	4.91	-12.95	8.60	-1.26	2.68	-14.69	14.81	-1.46	3.23
Buoy v	-53.12	46.01	-3.47	15.22	-26.65	40.13	3.91	8.30	-45.89	45.54	4.51	10.02
	R^2 u	**P-value**	**R^2 v**	**P-value**	**R^2 u**	**P-value**	**R^2 v**	**P-value**	**R^2 u**	**P-value**	**R^2 v**	**P-value**
	0.40	0.00	0.40	0.00	0.19	0.00	0.19	0.00	0.35	0.00	0.35	0.00
	Buoy R											
	Min	**Max**	**Mean**	**Std**	**Min**	**Max**	**Mean**	**Std**	**Min**	**Max**	**Mean**	**Std**
Buoy u	-11.80	7.61	-0.46	2.34	-12.31	8.77	-0.82	1.98	-13.15	13.74	0.17	2.55
Buoy v	-23.59	36.56	1.44	7.24	-27.19	38.16	2.53	6.13	-42.57	40.76	-0.52	7.90
	R^2 u	**P-value**	**R^2 v**	**P-value**	**R^2 u**	**P-value**	**R^2 v**	**P-value**	**R^2 u**	**P-value**	**R^2 v**	**P-value**
	0.11	0.00	0.11	0.00	0.09	0.00	0.09	0.00	0.21	0.00	0.21	0.00
	Buoy W											
	Min	**Max**	**Mean**	**Std**	**Min**	**Max**	**Mean**	**Std**	**Min**	**Max**	**Mean**	**Std**
Buoy u	-10.36	9.46	-1.49	3.19	-11.67	13.91	0.75	3.50	-16.40	14.92	0.62	3.83
Buoy v	-29.31	32.09	4.61	9.89	-43.10	36.22	-2.33	10.84	-46.23	50.83	-1.91	11.88
	R^2 u	**P-value**	**R^2 v**	**P-value**	**R^2 u**	**P-value**	**R^2 v**	**P-value**	**R^2 u**	**P-value**	**R^2 v**	**P-value**
	0.27	0.00	0.27	0.00	0.18	0.00	0.18	0.00	0.35	0.00	0.35	0.00

Table 4. Metrics for the zonal (u) and meridional (v) component of the SSDE radials and the projected buoy data in cm/s.

	SSDE Winter 2016-2017				SSDE Spring 2017				SSDE Summer 2016			
	Buoy B											
	Min	**Max**	**Mean**	**Std**	**Min**	**Max**	**Mean**	**Std**	**Min**	**Max**	**Mean**	**Std**
Radar u	-48.20	53.56	-5.38	17.06	-54.36	42.27	-8.50	16.60	-44.34	41.74	3.82	17.30
Radar v	-10.88	9.79	1.09	3.46	-8.59	11.04	1.73	3.37	-16.38	17.40	-1.50	6.79
Buoy u	-49.40	22.55	-16.24	13.92	-39.28	-1.33	-22.18	12.32	-44.33	30.02	-1.00	12.45
Buoy v	-4.58	10.03	3.30	2.83	0.27	7.98	4.50	2.50	-11.79	17.40	0.39	4.89
	R^2 u	**P-value**	**R^2 v**	**P-value**	**R^2 u**	**P-value**	**R^2 v**	**P-value**	**R^2 u**	**P-value**	**R^2 v**	**P-value**
	0.68	0.00	0.68	0.00	0.34	0.01	0.34	0.01	0.54	0.00	0.54	0.00
	Buoy F											
	Min	**Max**	**Mean**	**Std**	**Min**	**Max**	**Mean**	**Std**	**Min**	**Max**	**Mean**	**Std**
Buoy u	-43.52	45.97	-6.76	13.66	-51.04	34.52	-9.50	14.26	-33.75	47.554	5.2676	17.539
Buoy v	-9.34	8.84	1.37	2.77	-7.01	10.37	1.93	2.90	-18.66	13.248	-2.068	6.884
	R^2 u	**P-value**	**R^2 v**	**P-value**	**R^2 u**	**P-value**	**R^2 v**	**P-value**	**R^2 u**	**P-value**	**R^2 v**	**P-value**
	0.87	0.00	0.87	0.00	0.79	0.00	0.79	0.00	0.47	0.00	0.47	0.00
	Buoy R											
	Min	**Max**	**Mean**	**Std**	**Min**	**Max**	**Mean**	**Std**	**Min**	**Max**	**Mean**	**Std**
Buoy u	-49.43	36.55	-9.51	13.34	-50.60	40.70	-14.97	17.80	-44.47	33.32	-1.74	15.13
Buoy v	-7.42	10.04	1.93	2.71	-8.27	10.28	3.04	3.62	-13.08	17.45	0.68	5.94
	R^2 u	**P-value**	**R^2 v**	**P-value**	**R^2 u**	**P-value**	**R^2 v**	**P-value**	**R^2 u**	**P-value**	**R^2 v**	**P-value**
	0.61	0.00	0.61	0.00	0.45	0.00	0.45	0.00	0.31	0.00	0.31	0.00
	Buoy W											
									Min	**Max**	**Mean**	**Std**
Buoy u									-40.83	34.20	-2.55	13.25
Buoy v									-13.43	16.03	1.00	5.20
									R^2 u	**P-value**	**R^2 v**	**P-value**
									0.55	0.00	0.55	0.00

Table 4. Continued.

	SSDE Summer 2017				SSDE Fall 2016				SSDE Fall 2017			
	Buoy B											
	Min	**Max**	**Mean**	**Std**	**Min**	**Max**	**Mean**	**Std**	**Min**	**Max**	**Mean**	**Std**
Radar u	-69.59	82.72	7.57	22.47	-51.54	28.69	-16.96	11.85	-54.25	45.16	-15.22	17.22
Radar v	-16.8	14.13	-1.54	4.56	-5.83	10.47	3.44	2.41	-9.17	11.02	3.09	3.5
Buoy u	-47.24	47.33	2.14	20.04	-46.56	15.28	-17.76	11.54	-45.7	20.96	-9.51	11.48
Buoy v	-9.61	9.59	-0.44	4.07	-3.1	9.46	3.61	2.34	-4.26	9.28	1.93	2.33
	R^2 u	**P-value**	**R^2 v**	**P-value**	**R^2 u**	**P-value**	**R^2 v**	**P-value**	**R^2 u**	**P-value**	**R^2 v**	**P-value**
	0.45	0	0.45	0	0.23	0	0.23	0	0.31	0	0.31	0
	Buoy F											
	Min	**Max**	**Mean**	**Std**	**Min**	**Max**	**Mean**	**Std**	**Min**	**Max**	**Mean**	**Std**
Buoy u	-46.32	49.6	6.77	16.04	-48.75	14.17	-13.81	10.53	-54.22	37.28	-15	12.82
Buoy v	-10.07	9.41	-1.37	3.26	-2.88	9.9	2.8	2.14	-7.57	11.01	3.05	2.6
	R^2 u	**P-value**	**R^2 v**	**P-value**	**R^2 u**	**P-value**	**R^2 v**	**P-value**	**R^2 u**	**P-value**	**R^2 v**	**P-value**
	0.66	0	0.66	0	0.47	0	0.47	0	0.59	0	0.59	0
	Buoy R											
	Min	**Max**	**Mean**	**Std**	**Min**	**Max**	**Mean**	**Std**	**Min**	**Max**	**Mean**	**Std**
Buoy u	-52.13	45.03	-2.9	15.33	-52.76	6.93	-10.36	8.67	-47.95	49.76	-11.52	14.62
Buoy v	-9.15	10.59	0.59	3.11	-1.42	10.72	2.1	1.76	-10.11	9.74	2.34	2.97
	R^2 u	**P-value**	**R^2 v**	**P-value**	**R^2 u**	**P-value**	**R^2 v**	**P-value**	**R^2 u**	**P-value**	**R^2 v**	**P-value**
	0.46	0	0.46	0	0.15	0	0.15	0	0.56	0	0.56	0
	Buoy W											
	Min	**Max**	**Mean**	**Std**	**Min**	**Max**	**Mean**	**Std**	**Min**	**Max**	**Mean**	**Std**
Buoy u	-47.64	46.78	0.62	18.13	-48.75	25.13	-15.79	13.36	-51.72	48.59	-14.12	16.85
Buoy v	-9.5	9.68	-0.13	3.68	-5.1	9.9	3.21	2.71	-9.87	10.50	2.87	3.42
	R^2 u	**P-value**	**R^2 v**	**P-value**	**R^2 u**	**P-value**	**R^2 v**	**P-value**	**R^2 u**	**P-value**	**R^2 v**	**P-value**
	0.44	0	0.44	0	0.2	0	0.2	0	0.49	0	0.49	0

3.2 Seasonality of Data Availability

The HF radar footprint of data is given by the intersection of the data output from the RLVR and SSDE. A typical output for RLVR is shown in the methods section. The general data availability pattern showed that data cells offshore to RLVR rapidly lose data concentration as we move away from the coast, while the cells off to SSDE tend to preserve high data concentration further offshore. Yet, the region perpendicular to the midpoint between RLVR and SSDE conserves high data concentration as far as the HF radar range reached, and the data point with maximum data available (point used for methods such as wavelet and coherence) is located straight from the so-called midpoint halfway from the total range of the footprint. The decrease of data offshore coincides with the area with the increase in variance (see variance ellipses distribution in the next section).

The total of points collected through the time series analyzed consists of 11306 hours data (up to 471 days of data, close to 15 months and 13 days). To better assess the performance of the HF radar, the data availability color maps are classified per season to determine the seasonal data density (Figure 16, a–f). To estimate the percentage of coverage, the total number of measurements collected on a certain season, was divided by the maximum, i.e., the data was normalized per season.

Winter of 2016–2017 (Figure 16, a) was the second largest record (up to 2144 data points ~ 89 days), with marked gradients in the data availability distribution. Note that the variance increased from fall to winter, maybe due to the front passages that occur during winter. Nonetheless, the gradients on data available during the winter are not as high as during the spring.

Spring 2017 (Figure 16, b) season with the smallest salinity, has the steepest gradient on the data availability (up to 2040 data points – 85 days), coinciding with the marked variance fluctuations (see variance ellipses map).

During the summer of 2016 (up to 1821 data points ~ 76 days, Figure 16, c; and summer of 2017 (up to 1581 data points ~ 65 days, Figure 16, d) the changes in data availability smooth down compared to spring. However, the data saturation gradient is not as homogeneous as the observed during the fall. The near-uniform gradient is possibly related to the high variance within the data cloud, a result of the high energy brought by the flow reversal that transports saline water from Mexico to the Texas shelf, enhancing the performance of the HF radar.

Given that during the fall the freshwater input is the annual smallest, the data availability during the fall of 2016 (Figure 16, e) and fall of 2017 (Figure 16, f) exhibited a nearly uniform distribution. Yet, the pattern of a decrease in data available on the east and southwest of the data coverage was persistent. The fall of 2016 was the season with maximum data available (up to 2184 data points – 91 days) and measured the smallest variance (see variance ellipses map) of the record, presumably favoring the smooth gradient of changes on data available throughout the area resolved by the HF radar. The fall of 2017 measured the shortest time series (up to 1564 data points ~ 65 days).

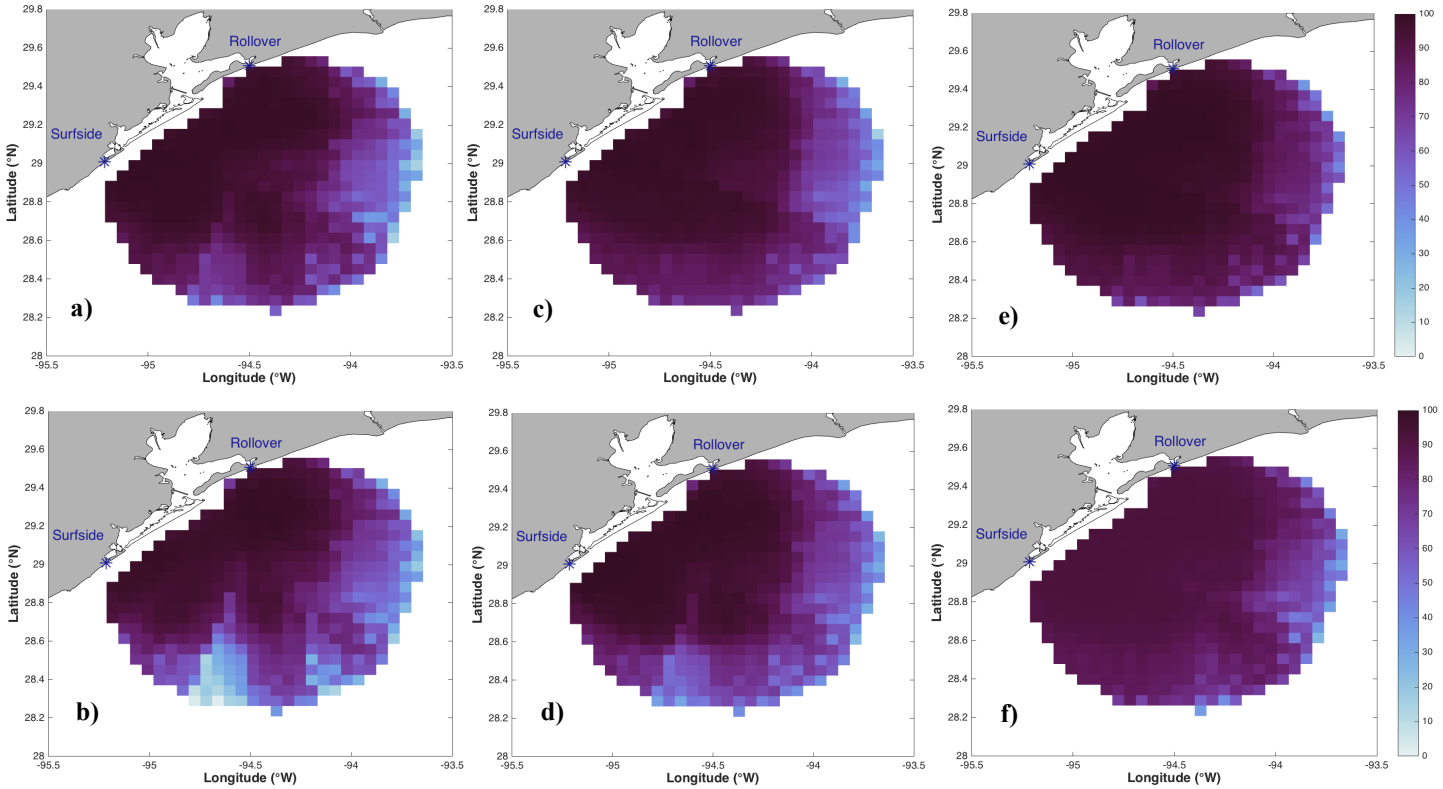

Figure 16. Spatial distribution of data measured from RLVR and SSDE for a) Winter, b) Spring, c) Summer 2016, d) Summer 2017, e) Fall 2016 and f) Fall 2017. The colorbar represents the percent of measurements collected. The maximum percentage is represented with dark purple, decreasing to light blue.

From the color maps above, there are repeated patterns where the radar did not collect measurements, e. g., south of the footprint between -95ºW and -94.5ºW and east of the footprint between 28.8ºN and 29.5ºN, that due to its persistence regardless of the environmental conditions, the causes of this data gaps are associated with problems with the instrument itself. Figure 17 shows an overlap of the RLVR and SSDE radials over the active oil and gas leases as of June of 2018, indicating that there are some platforms located near the sites and potentially attenuating the propagation of the electromagnetic signal, or impeding it idea propagation path. Regarding the oil and gas platforms, it would be ideas to know what specific type of operations are taking place on each active oil and gas lease to understand better the external noise that could be added to the HF radar system. Figure 17 also shows an overlap of the radials over the commercial vessel density, data as of 2010, where the radials with the least data from RLVR coincide with one of the waterways with higher vessel density. The navigation system of some vessels is contained within the operating frequency of the HF radar, and as the ships move toward and away from the coast, it could be a potential source of noise to the HF radar signal. These sources of noise could potentially be attenuated by changes in the atmospheric refraction index, which has seasonal changes and could change the bending of the electromagnetic wave on its way back to the surface. However, these atmospheric changes are not addressed in this thesis.

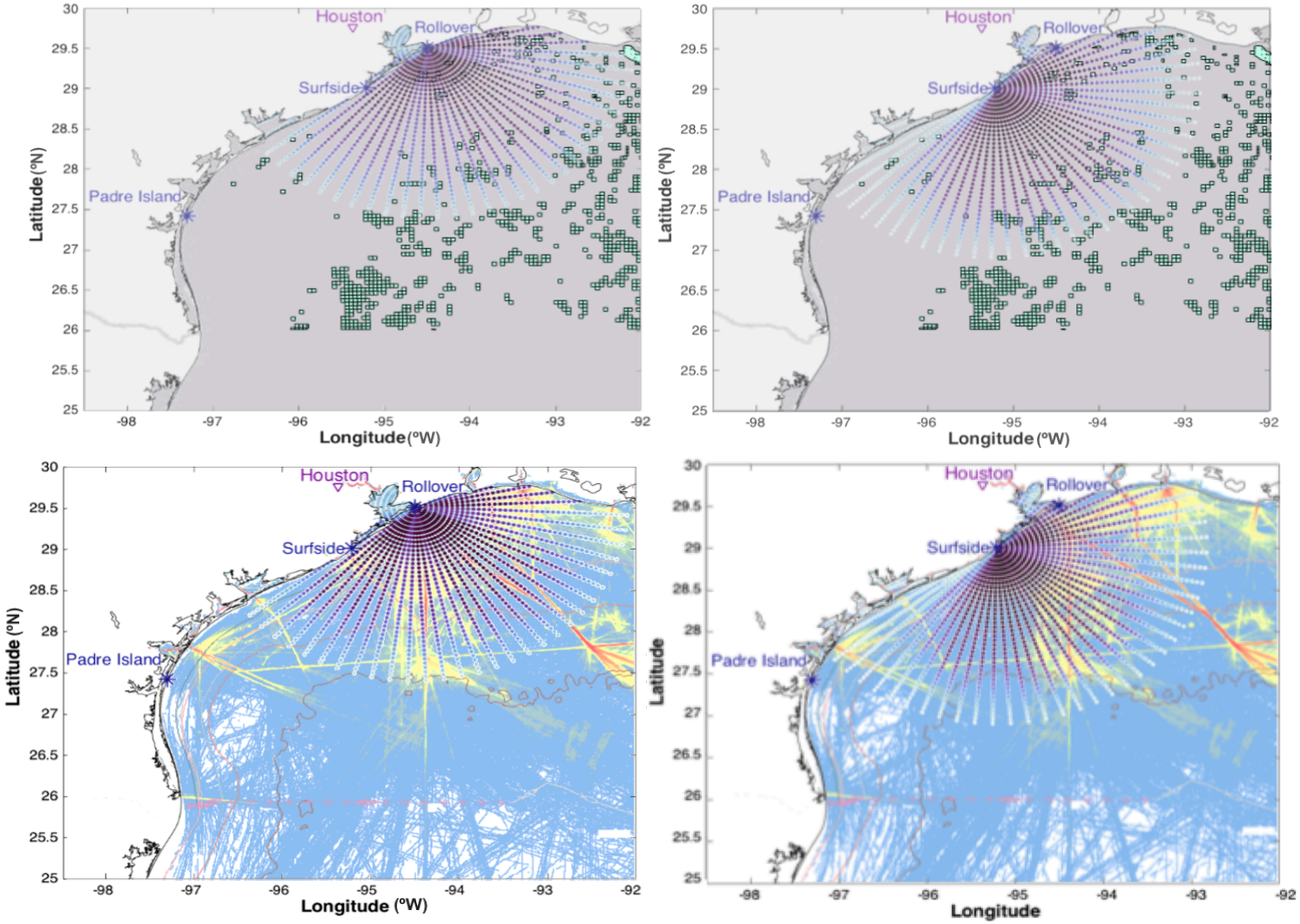

Figure 17. (Top) RLVR (left) and SSDE (right) radials over the active oil and gas leases (green squares). (Bottom) RLVR (left) and SSDE (right) radials over commercial vessel density, where red (blue) colors represent high vessel density.

3.3 Variance Ellipses

The variance ellipses have a predominant northeast-southwest (NE-SW) direction for all the seasons, a result of the dominant wind-driven circulation, with a component either upcoast or downcoast, but parallel to the coast (alongshore). Concretely, winter 2016–2017 and fall 2017 have east-northeast (ENE) trend, while the rest of the seasons have north-northeast (NNE) disposition. Summer 2017 is the season with ºthe most variance (mean minor axis 0.0202 m2/s2 and mean major axis 0.0691 m2/s2), followed by summer 2016, season with a notable increase in the variance off of the 20 m isobath, and then by spring. Fall 2016 is the season with the least variance (mean minor axis 0.0073 m2/s2 and mean major axis 0.0200 m2/s2), followed by winter 2016–2017 and fall 2017 (in that order). The ellipses of fall 2016 are nearly circular, suggesting that the variance along and across the shelf was similar during the months in this season. Table 5 summarizes the seasonal ranges of the minor axes, major axes, and angles of the variance ellipses per season

For all the seasons, the ellipses closer to the shore are anisotropic with a cross-shore pattern. The reason for the anisotropy of the ellipses very close to the coast is that the angle between the radials from both sites is near parallel. The closer to an orthogonal relationship between radials, the better the measurements will be. Similarly, due to the curvature of the coastline and its effect on the angle between radials, on the northeast edge of the data cloud, closer to Rollover, the ellipses are oriented north-south (N-S). Generally, the ellipses observed were more elongated on the edges and as we move offshore (closer to the 50m isobath), related with a decrease in the signal intensity given by the HF radar range.

Variance ellipses tend to follow the curvature of the 50 m isobath, the observed trend agrees with the findings of Nowlin et al. (2005), who suggest that the shelf is divided at approximately the 50-m isobath. The inner shelf comprises the area from the coast to the 50-m isobath, where the weather band predominates reflecting the effect of frequent frontal passages over the region. The outer shelf is the region that comes after the 50-m isobath, where the mesoscale band, i.e., eddies, dominates and characterizes the circulation of this region.

Areas with the highest variance followed the pattern of the area with fewer data collected. Having fewer data measured by the HF radar limits its capability of having enough redundancy to estimate accurate measurements, and that is reflected on the increase of variance ellipses. Figure 18 shows a color map of the spatial distribution of the major axis in m^2/s^2 for spring. Note how the yellowish patches of larger major axes on Figure 18 resemble those light blue patches on Figure 16, b.

The variance ellipses are related with the regional bathymetry. Figure 19 shows a 3D representation of the bathymetry, where it is possible to observe that on the side of SSDE the depth changes faster than on the side of RLVR. Figure 20 shows a 2D representation of the depth and the estimated depth gradient within the HF radar footprint using a high-resolution bathymetry. The depth gradient offshore from SSDE is steeper than that offshore from RLVR, where color saturation represents those regions with strong depth gradients. The depth gradient moving offshore from SSDE is 0.33, with a change in depth from 18 m corresponding to its nearest radar point to 52 m deep on its furthest perpendicular radar point (located 100.8 km offshore). For RLVR, the depth gradient is 0.11, with shallowest radar point located on the 11 meters depth contour and

the furthest was 24 meters (located 110.7 km offshore). The deepest location within the HF radar footprint was 56 m deep, and the shallowest was 10 m deep.

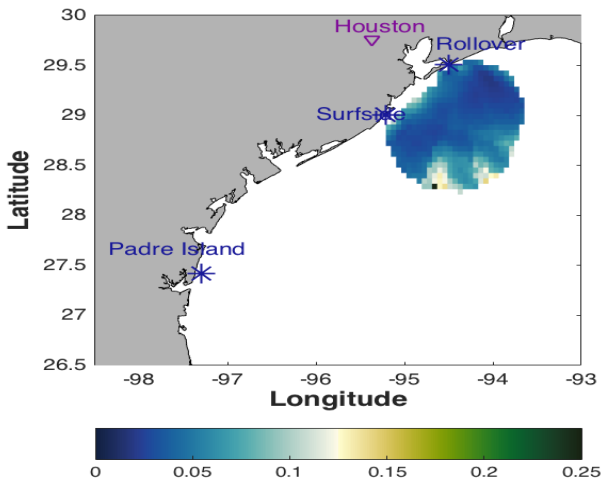

Figure 18. Color map of variance major axis for spring in m2/s2, where the size of the major axis increases from blue to green.

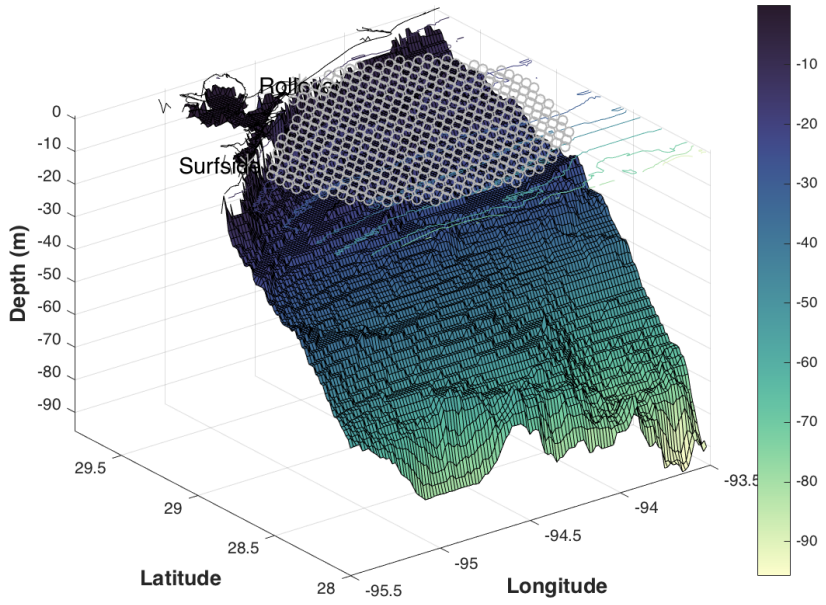

Figure 19. Three dimensional representation of the local bathymetry. Light (dark) colors represent deeper (shallower) locations. The HF radar footprint is represented on top.

Although the steepest slope is located offshore surfside, Figure 20 shows a distinctive strong gradient parallel to the coast between -94.6ºW and -94ºW, which coincidently marked a transition zone, resulting in an increase in the size of the variance ellipses.

The ratio minor axis to major axis gives information about the oblateness of the variance ellipses. A ratio close to 1 corresponds to rounded ellipses and small ratios are associated with elongated ellipses (major axis >> minor axis). Figure 21 represents the variance ellipses in the HF radar footprint and color maps that represent the spatial distribution of the ration of minor axis to major axis.

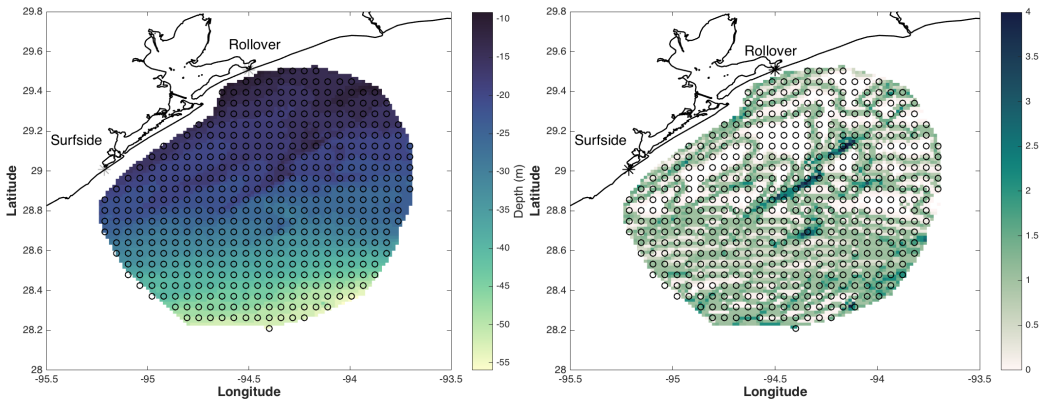

Figure 20. (Left) Two dimensional color map that represents the changes in bathymetry for the HF radar footprint. Light (dark) colors represent deeper (shallower) locations. (Right) Depth gradient within the HF radar footprint from high-resolution bathymetry. The depth gradient increases with the color. Near SSDE the depth gradient is steeper than the gradient close to RLVR. But the strongest gradient is located parallel to the coastline. The open circles indicate locations where the radar made a measurement.

Table 5. Summary of the minimum (min), maximum (max), mean, and standard deviation (std) of the minor axis, major axis, and angle, per season. The mean angle is written in radians and degrees to ease the interpretation.

	Minor Axis (m^2/s^2)				Major Axis (m^2/s^2)				θ (rad)				θ (º)
	Min.	**Max.**	**Mean**	**Std.**	**Min.**	**Max.**	**Mean**	**Std.**	**Min.**	**Max.**	**Mean**	**Std.**	**Mean**
Winter 2016–2017	0.0035	0.0464	0.0107	0.0038	0.0167	0.0669	0.0319	0.0079	–1.4997	1.5364	0.2871	0.2730	16.4508
Spring 2017	0.0047	0.0538	0.0140	0.0037	0.0188	0.2476	0.0478	0.0229	–1.5560	1.5026	0.5806	0.3603	33.2642
Summer 2016	0.0044	0.0551	0.0185	0.0069	0.0235	0.1924	0.0690	0.0264	–1.3219	1.5354	0.5475	0.1858	31.3706
Summer 2017	0.0026	0.0498	0.0202	0.0061	0.0289	0.1843	0.0691	0.0220	–1.5512	1.3382	0.5442	0.2561	31.1809
Fall 2016	0.0040	0.0199	0.0073	0.0019	0.0097	0.0524	0.0200	0.0052	–1.5592	1.5592	0.4858	0.3918	27.8366
Fall 2017	0.0047	0.0387	0.0108	0.0029	0.0177	0.0827	0.0393	0.0109	–1.5564	1.5583	0.4076	0.2630	23.3526

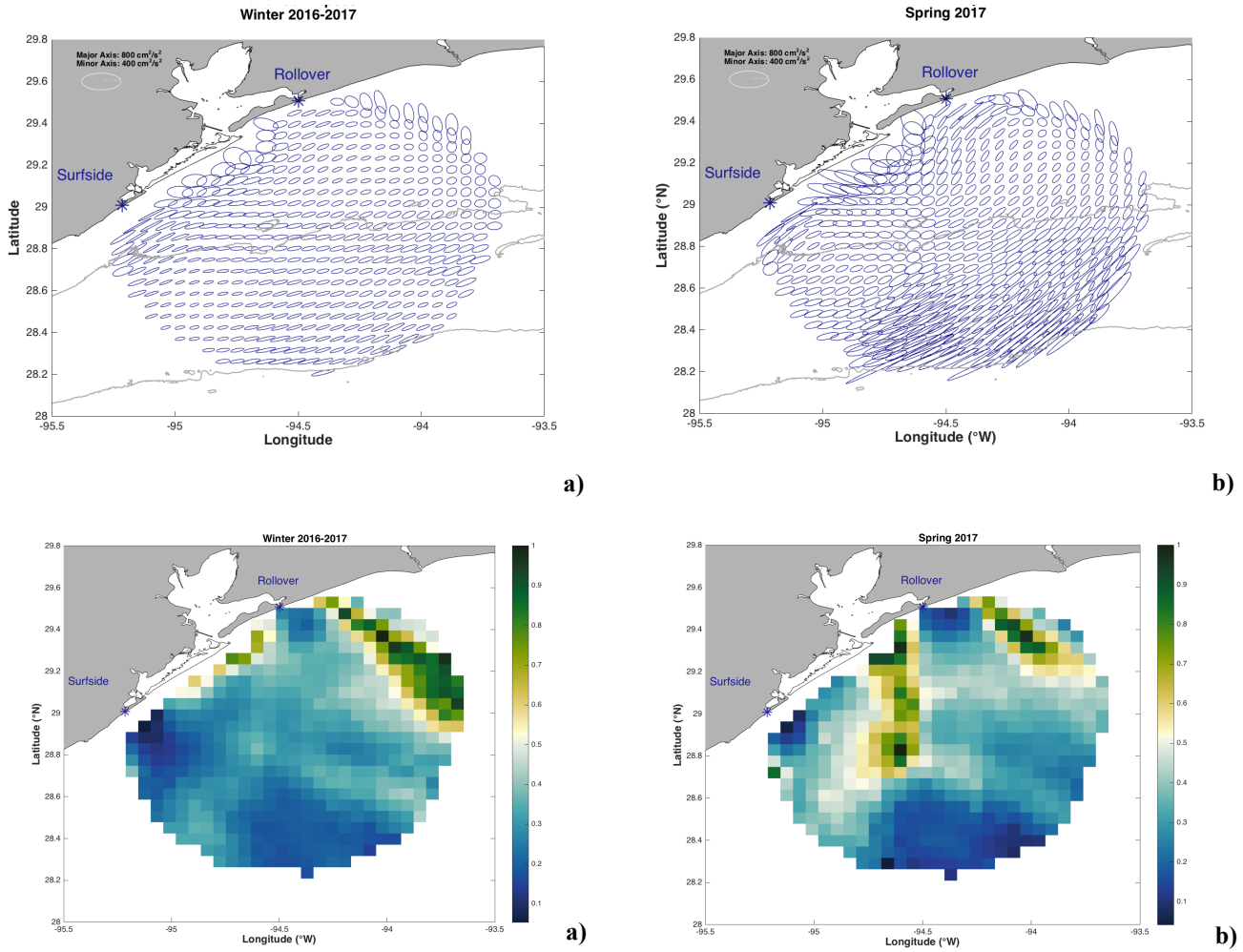

Figure 21. (Top) Variance ellipses in cm^2/s^2 with 20m and 50m bathymetric contours and (bottom) m/M ratio, where the green (blue) colors represent rounded (oblate) ellipses, for the a) Winter, b) Spring, c) Summer 2016, d) Summer 2017, e) Fall 2016, and f) Fall 2017.

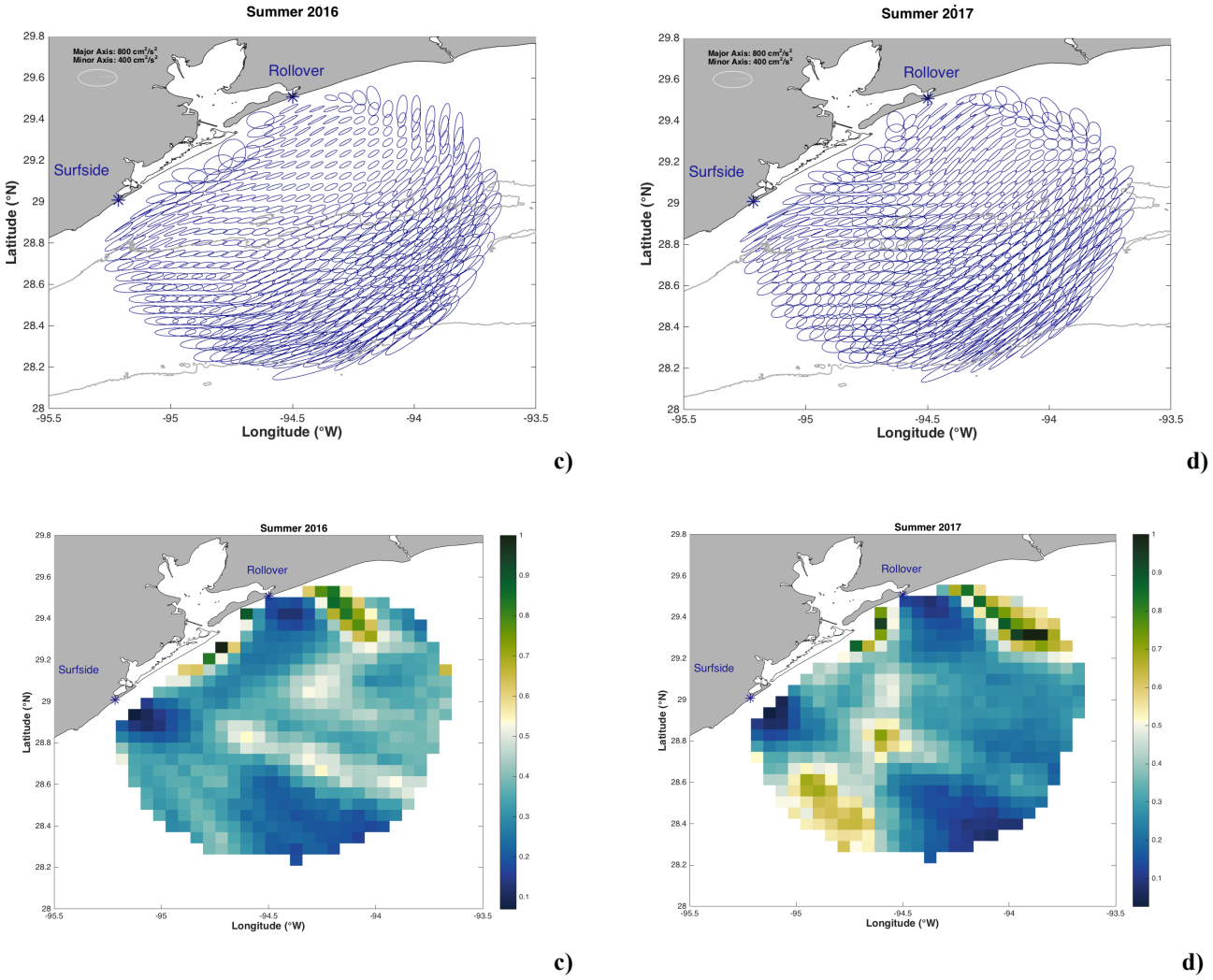

Figure 21. Continued.

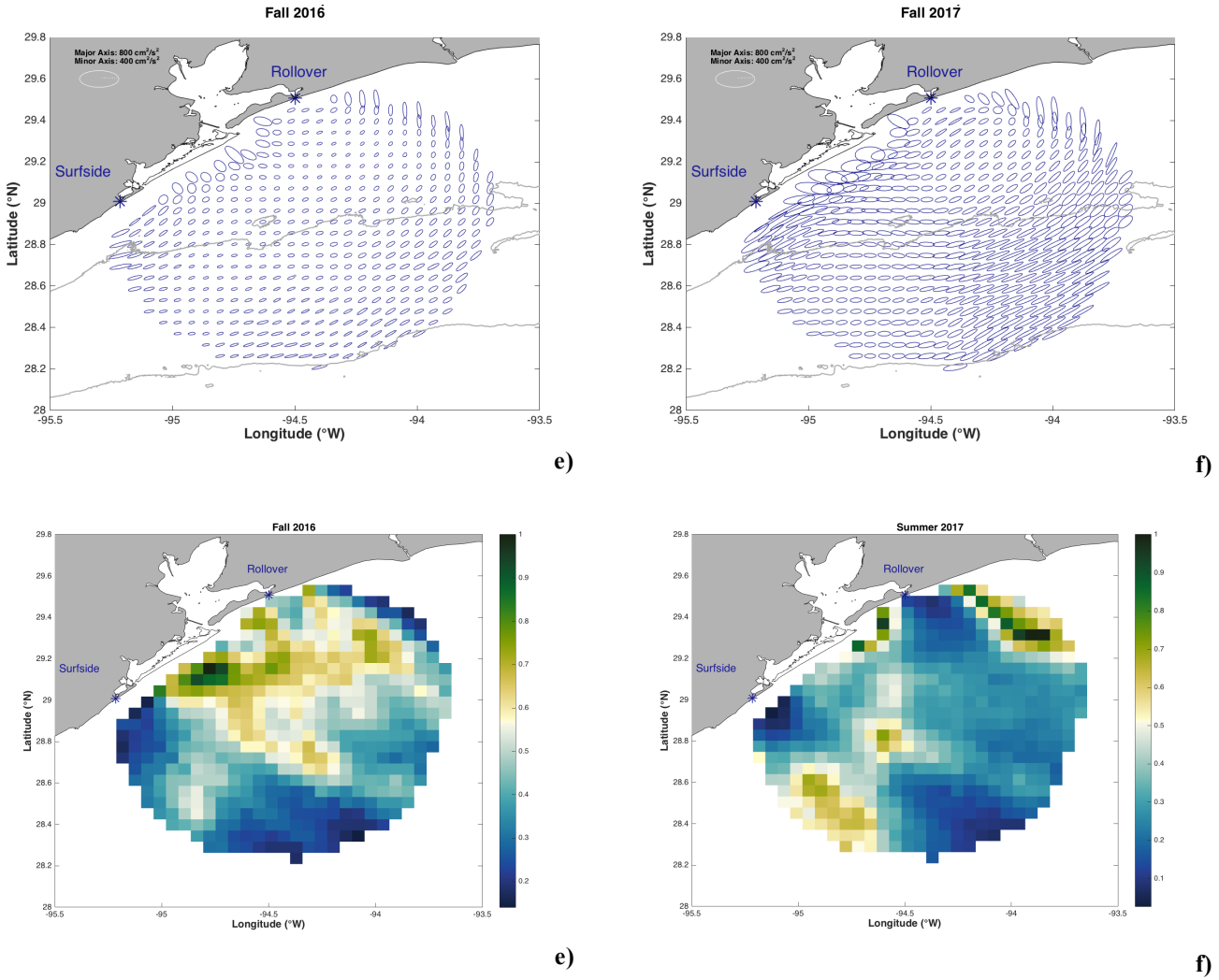

Figure 21. Continued.

3.4 Power Spectra

The rotation of the zonal and meridional component of the output velocity vector corresponding to the time series with the most data within the HF radar footprint, resulted in the alongshore and cross-shore component analyzed using power spectra. The power spectra of the alongshore and cross-shore component shows a notable increase in the power content in the diurnal and the semi-diurnal period (Figure 22, a–f). The only exceptions are the cross-shore component of spring (no energy peak for the diurnal frequency), and the alongshore component of summer 2017 (no clear peak on the semi-diurnal frequency). When smoothing the power spectra one can easily detect the diurnal and semi-diurnal peaks, which indeed, are contained within the 95% confidence interval.

Summer is the seasons with higher power density spectra, predominantly in the cross-shore component, for both, 2016 and 2017 (Figure 22, c, d). The high power content observed in the diurnal band during summer is attributed to the diurnal tides, the inertial oscillations (local inertial period of 24.78 hrs), and the near-resonant response to the sea breeze, which is enhanced during the summer due lto and-sea temperature gradients. The coastal sea-breeze with periods of 24 hrs. makes out of the summer a season thar responds easily to the local inertial period.

To remove the inertial oscillations a 40 hr. low-pass filter was applied. It is noticeable that the diurnal and semi-diurnal peaks are not exhibited and only the low frequencies remain. A theoretical -5/3 slope was overlap and compared with the seasonal low frequencies. The -5/3 slope represents the theoretical energy cascade. The similarity on the low frequency slopes on the power spectra compared to the -5/3 slope, show that the energy decay of the HF radar dataset is congruent with a theoretical energy cascade.

The cross-shore component of spring and the alongshore component of summer 2016, are the slopes that approximate the most to the -5/3 slope. Only the cross-shore slopes for summer 2016 and 2017 were steeper than -5/3, meaning that there is less energy in the weather band (2-15 days) due to a decrease in the number of frontal passages that occur during the summer. On the other hand, the slopes calculated during the winter and fall are similar among them and less steep than the -5/3, meaning that there is more energy in the weather band for these seasons as a result of the energy content in the weather band associated to a high number of frontal passages.

Winter (Figure 22, a):

Alongshore	Cross-shore
Diurnal density power: 20.17 (cm^2/s^2)/cpd	Diurnal density power: 36.63 (cm^2/s^2)/cpd
Semidiurnal density power: 4.45 (cm^2/s^2)/cpd	Semidiurnal density power: 23.1 (cm^2/s^2)/cpd
Low frequency slope: -1.40	Low frequency slope: -1.04

Spring 2017 (Figure 22, b):

Alongshore	Cross-shore
Diurnal density power: 33.7 (cm^2/s^2)/cpd	Diurnal density power: No peak
Semidiurnal density power: 10.07 (cm^2/s^2)/cpd	Semidiurnal density power: 21.49 (cm^2/s^2)/cpd
Low frequency slope: -0.98	Low frequency slope: -1.69

Summer 2016 (Figure 22, c):

Alongshore	Cross-shore
Diurnal density power: 42.88 (cm^2/s^2)/cpd	Diurnal density power: 86.25 (cm^2/s^2)/cpd
Semidiurnal density power: 12.8 (cm^2/s^2)/cpd	Semidiurnal density power: 18.04 (cm^2/s^2)/cpd

Low frequency slope: -1.70

Low frequency slope: -2.42

Summer 2017 (Figure 22, d):

Alongshore

Diurnal density power: 75.41 (cm^2/s^2)/cpd

Semidiurnal density power: No peak

Low frequency slope: -1.73

Cross-shore

Diurnal density power: 102.6 (cm^2/s^2)/cpd

Semidiurnal density power: 20.42 (cm^2/s^2)/cpd

Low frequency slope: -2.17

Fall 2016 (Figure 22, e):

Alongshore

Diurnal density power: 50.66 (cm^2/s^2)/cpd

Semidiurnal density power: 11.64 (cm^2/s^2)/cpd

Low frequency slope: -1.14

Cross-shore

Diurnal density power: 22.21 (cm^2/s^2)/cpd

Semidiurnal density power: 21.06 (cm^2/s^2)/cpd

Low frequency slope: -1.38

Fall 2017 (Figure 22, f):

Alongshore

Diurnal density power: 22.21 (cm^2/s^2)/cpd

Semidiurnal density power: 4.28 (cm^2/s^2)/cpd

Low frequency slope: -1.41

Cross-shore

Diurnal density power: 20.36 (cm^2/s^2)/cpd

Semidiurnal density power: 17.9 (cm^2/s^2)/cpd

Low frequency slope: -1.8

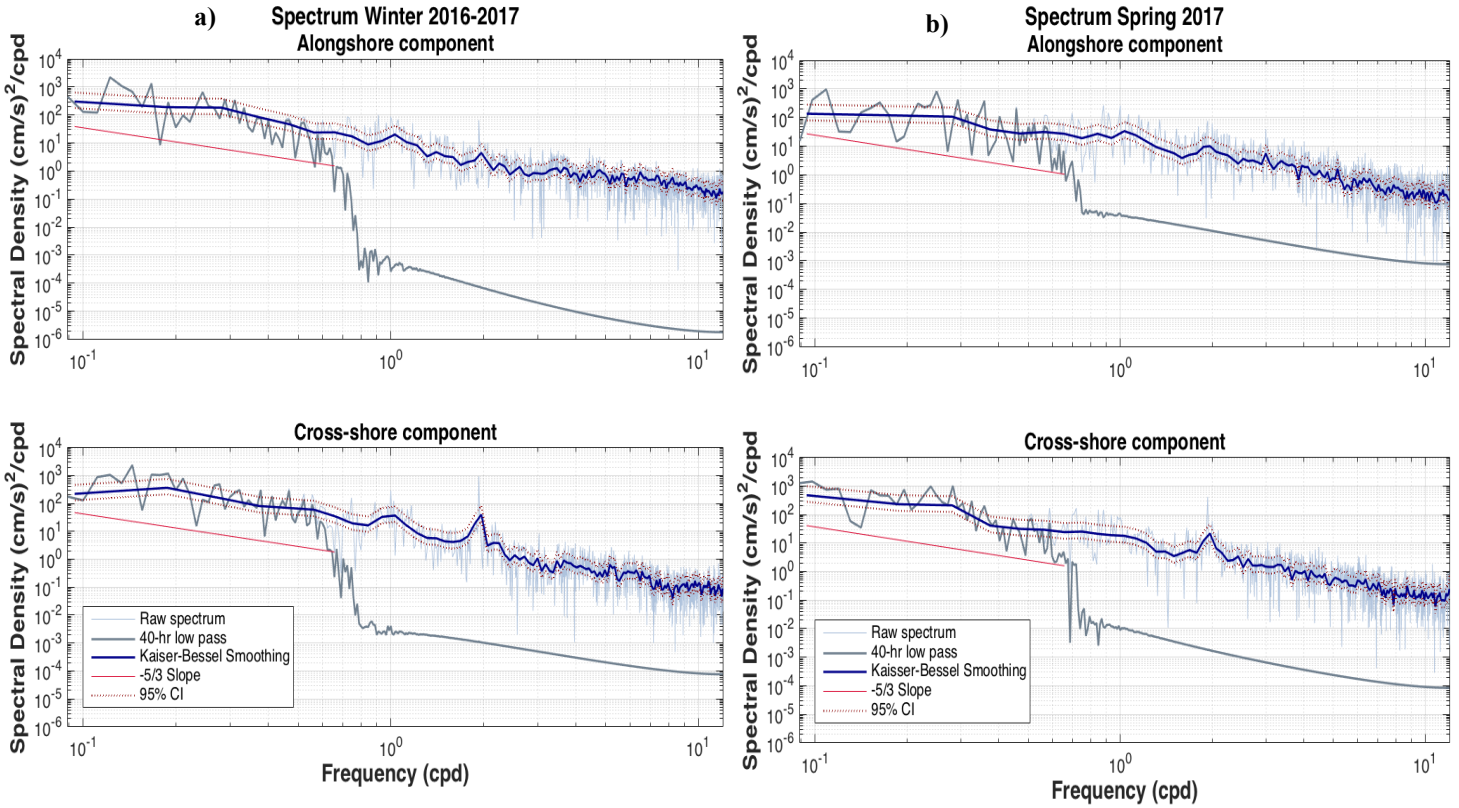

Figure 22. Alongshore (top) and cross-shore (bottom) power density spectra for a) Winter, b) Spring, c) Summer 2016, d) Summer 2017, e) Fall 2016, and f) Fall 2017. The light blue line represents the raw data, smoothed with a Kaiser-Bessel filter (dark blue) and enveloped by the 95% confidence interval (red dotted lines). The thick gray line represents the 40-hr low-passed data, and the red line on the low frequencies is the -5/3 Kolmogorov reference line.

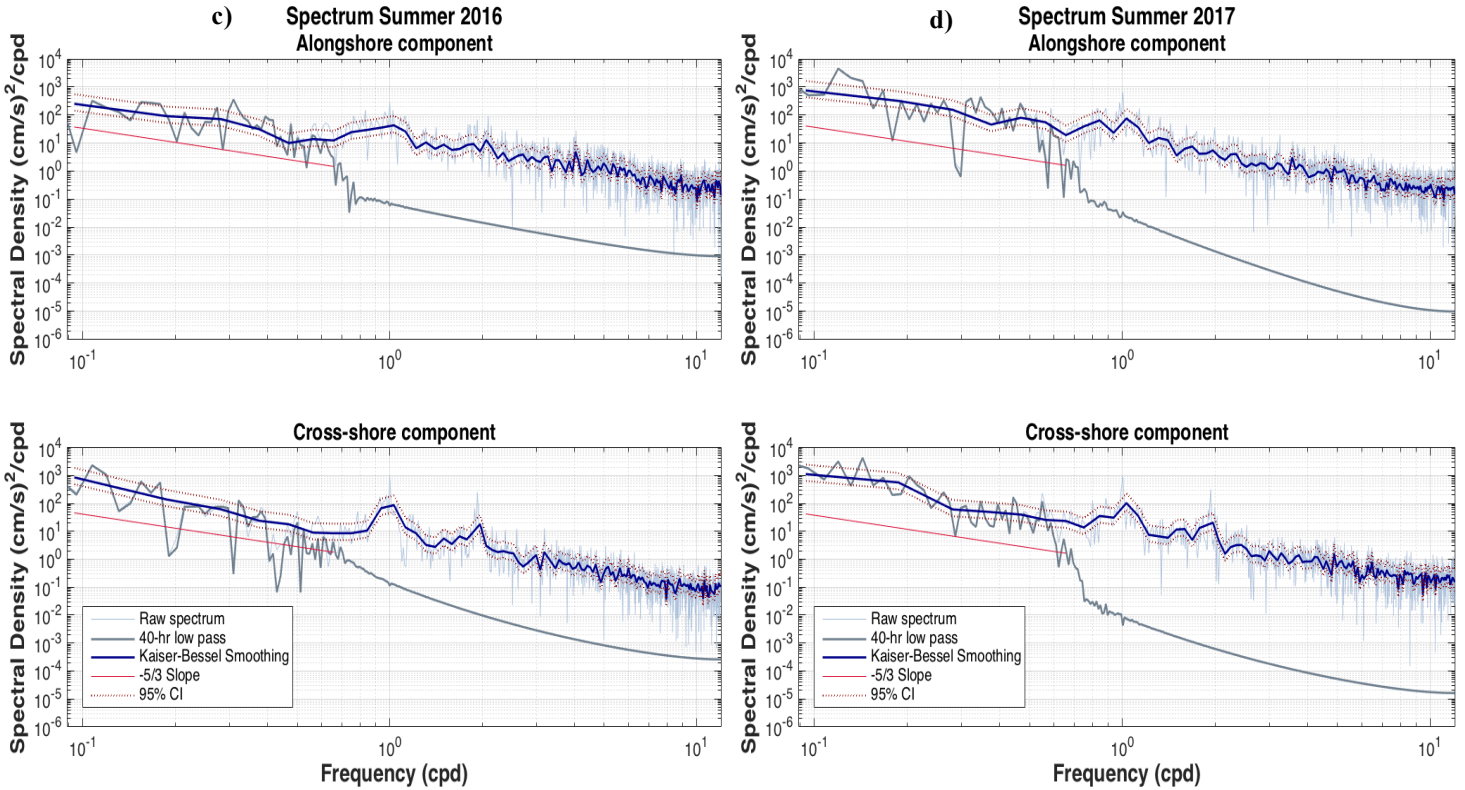

Figure 22. Continued.

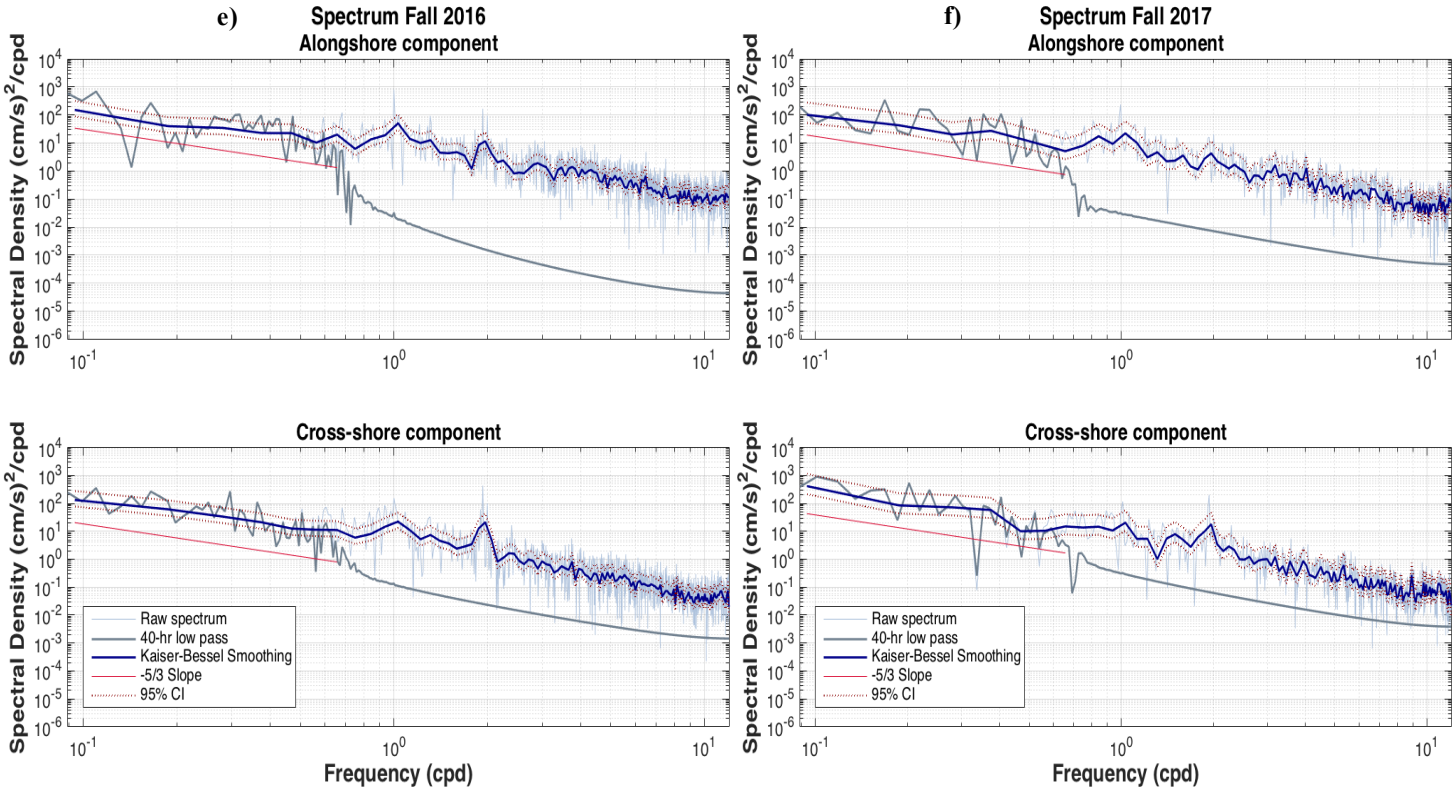

Figure 22. Continued.

3.5 Tidal Analysis

Spectral analysis of the output form the method of cyclic descent was analyzed using the alongshore and cross-shore components of the full dataset and the dataset with summers removed to compare it with the results of DiMarco and Reid (1998), and to reduce the effects of the near-resonant response to sea breeze with a period of 24 hrs.

A power spectrum from the raw and detided record helps to determine the principal diurnal and semidiurnal constituents. When the record is detided using the MCD it is possible to observe that only the tidal frequencies show a decrease in the power while the rest of the record remains nearly the same.

When analyzing the full dataset (summers included), the principal diurnal tidal constituents are O1, P1 and K1, with higher energy content associated to P1 and K1 (Figure 23), and the principal semi-diurnal constituents are M2 and S2, with higher power on M2 (Figure 25). In agreement to the maximum power content measured with the power spectra, when using the minor and major axis of the tidal ellipses to estimate the magnitude of the tidal ellipses, K1 and M2 are the dominant diurnal and semi-diurnal constituents, respectively. Table 6 lists the average mean of the minor and major tidal ellipses axes, including summers.

When analyzing the dataset with summer months removed, the principal diurnal constituents are O1 and K1 (Figure 24), and M2 and S2 remain being the dominant semi-diurnal constituents (Figure 26). P1 has a period very close to 24 hrs., and therefore, the forcing of the near-resonant response to sea-breeze during the summer might enhance the tidal amplitude at this period.

In general, the main tidal constituents found in this thesis are O1, P1, K1, M2, and S2, in agreement to DiMarco and Reid (1998). Similar to the observations of DiMarco and Reid (1998), the diurnal constituents tend to trace circular ellipses and the semidiurnal constituents tend to trace oblate ellipses (Figure 27). The sign of the minor axis gives the sense of rotation. When the minor axis is negative, the rotation is anticyclonic (clockwise) and when the minor axis is positive, the rotation is cyclonic (counter-clockwise). Figure 27 shows a color map of the normalized minor axis, where it is possible to observe that there is a predominant anticyclonic rotation (dominant negative minor axis), common in the northern hemisphere. M2 and S2 are the only tidal constituents that show some cyclonic rotation near the shore.

Tidal ellipses traced using the full dataset (summer included) show that the size of the tidal ellipses increases offshore, being K1 the constituent with the largest tidal ellipses. Although ellipses increase offshore, K1 ellipses near the coast are not notable small and have a cross-shore orientation. Although P1, in general, has larger ellipses than O1, closer to the coast O1 showed persistence on the size of the ellipses instead of rapidly decaying in size as P1. Between the 20 and 50-m isobaths, the diurnal tidal ellipses tend to follow the isobaths (K1 and P1).

M2 is the semi-diurnal constituent with the largest tidal ellipses. The ellipses straight offshore from SSDE, and that are constrained by the 20 and 50-m isobaths, tend to follow the bathymetry. Moving east, M2 shows a strong alongshore orientation between the coast and the 20-m isobath. For this constituent, most of the ellipses are oriented alongshore, with a narrow band of ellipses following the bathymetric contours. Ellipses near the shore are narrower and start increasing their minor axis offshore. The

ellipses of S2 are narrower (smaller minor axes compared to M2) and show an anisotropic distribution with three principal orientation components: alongshore, cross-shore and parallel to the isobaths. The band that contains ellipses parallel to the isobaths is the same as the observed on K1, P1, and M2. S2 ellipses decrease on the edges of the HF radar footprint.

Table 6. Range of the minor and major tidal ellipses axes, including summers

	Mean Major Axis (cm/s)	**Mean Minor Axis (cm/s)**
M2	2.88	-0.42
S2	1.11	-0.02
N2	0.75	-0.006
K2	0.35	-0.06
K1	4.67	-2.84
O1	2.57	-1.4
P1	3.01	-1.7
Q1	0.78	-0.36

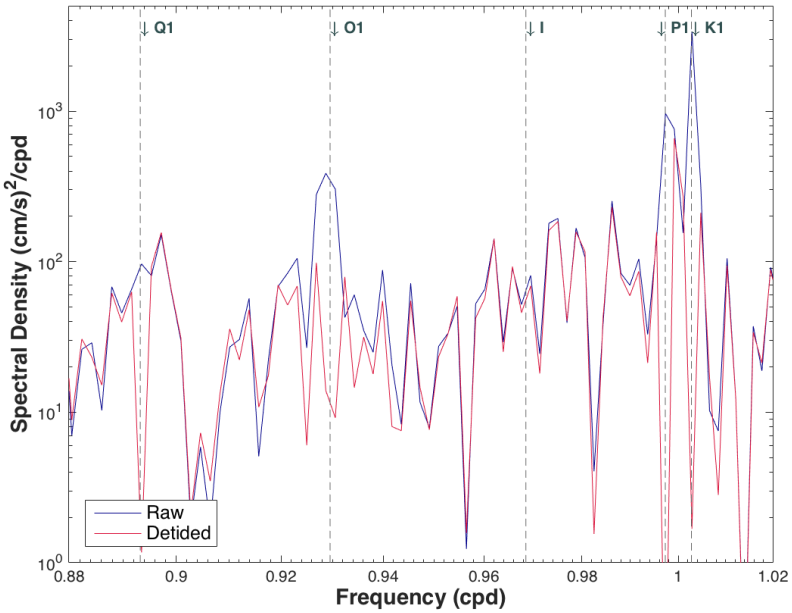

Figure 23. Power spectrum of diurnal tidal constituents and local inertial period (I), for the raw (blue) and detided (red) record for the full HF radar dataset.

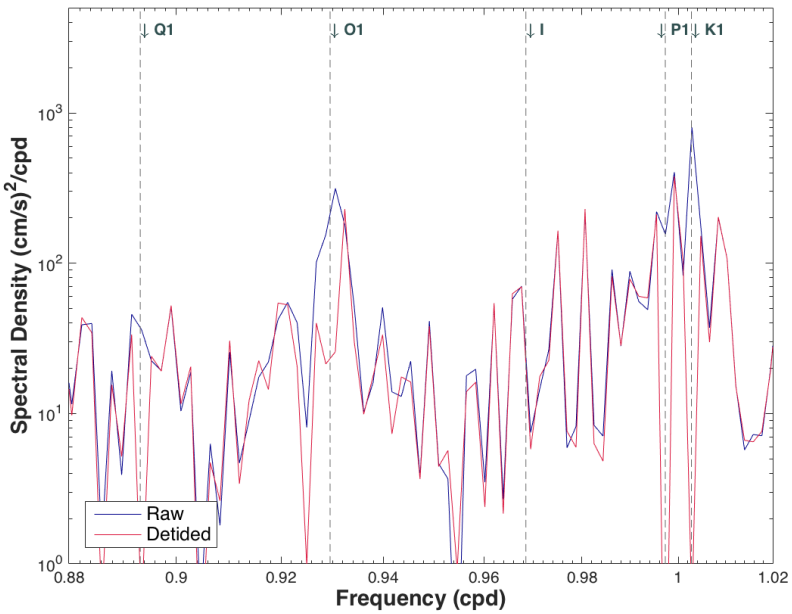

Figure 24. Power spectrum of diurnal tidal constituents and local inertial period (I), for the raw (blue) and detided (red) record for the HF radar dataset with summers removed.

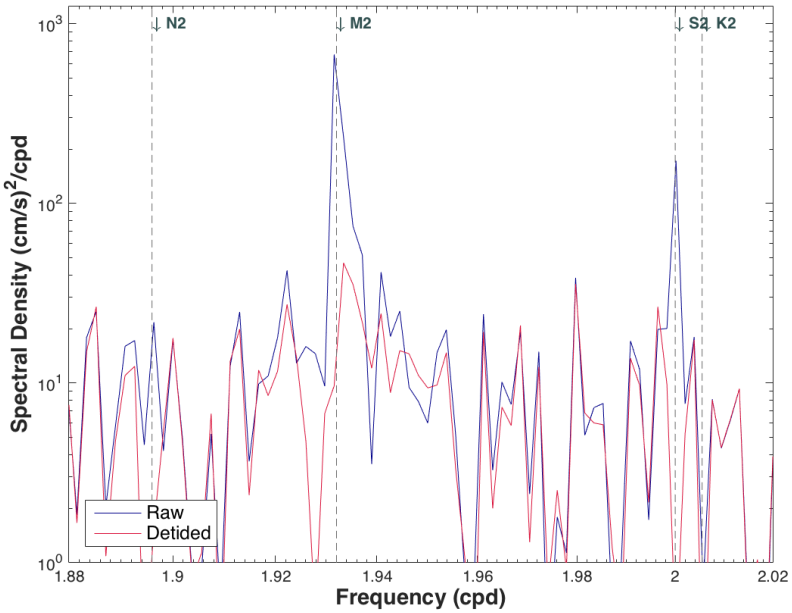

Figure 25. Power spectrum of semi-diurnal tidal constituents, for the raw (blue) and detided (red) record for the full HF radar dataset.

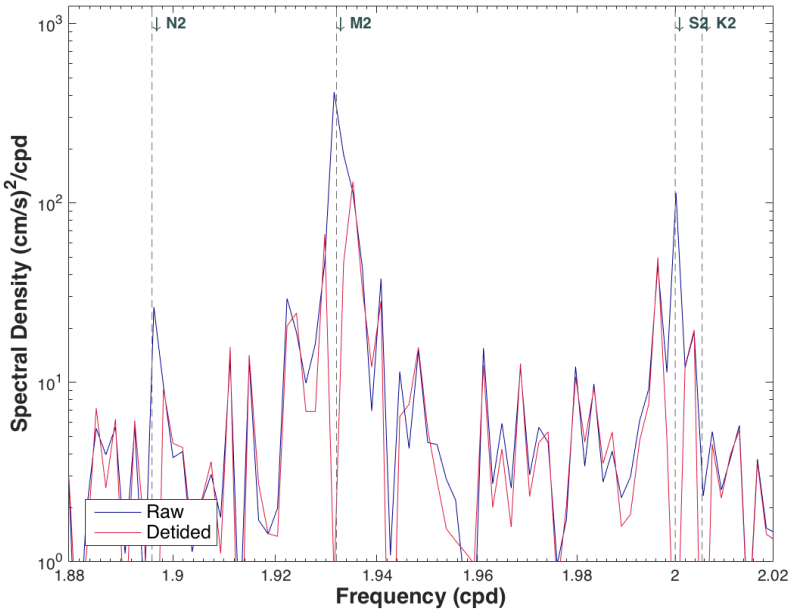

Figure 26. Power spectrum of semi-diurnal tidal constituents, for the raw (blue) and detided (red) record for the HF radar dataset with summers removed.

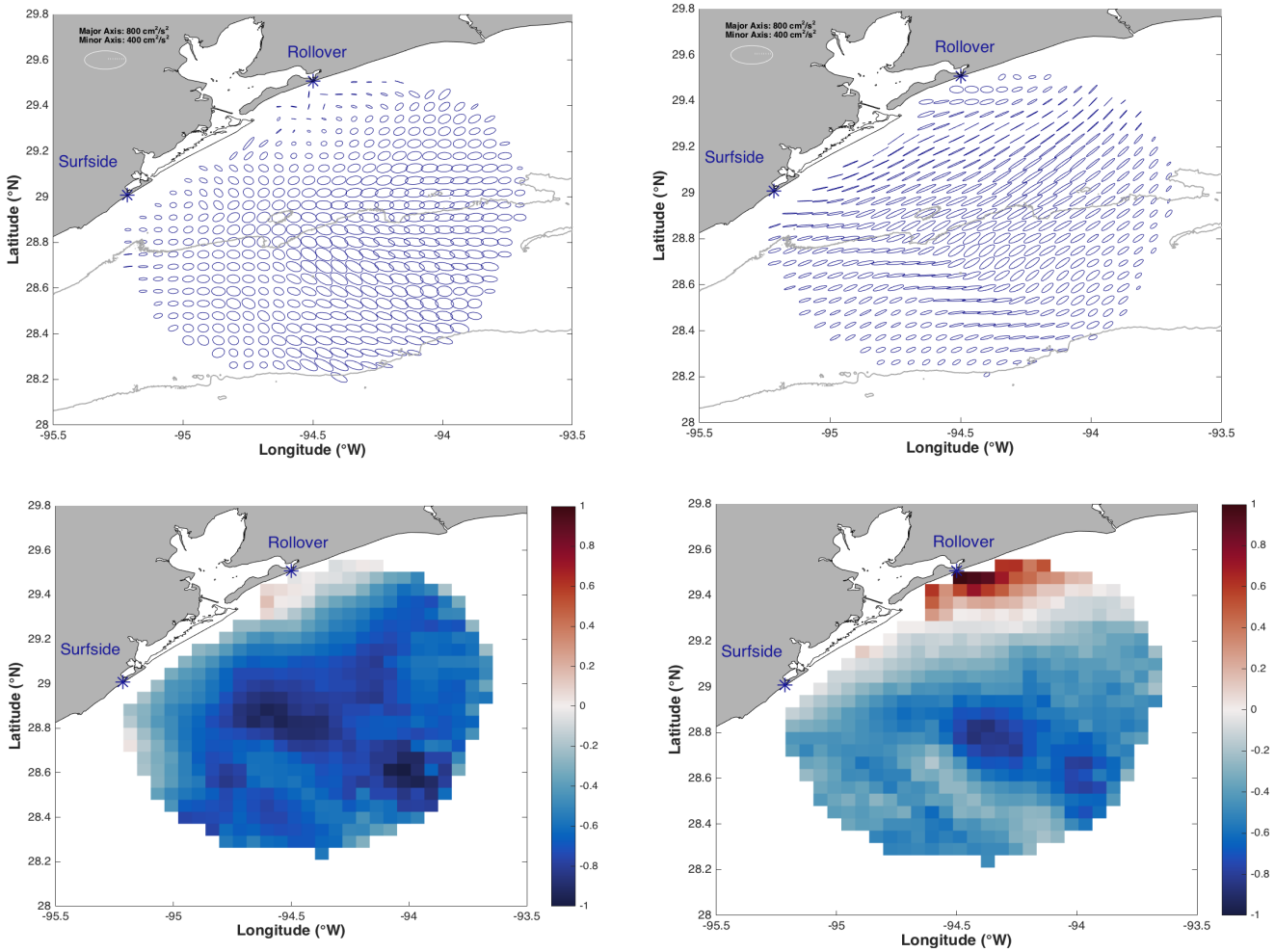

Figure 27. (Left) Diurnal O1 and (right) semi-diurnal M2 (top) tidal ellipses over the 20m and 50m bathymetric contours and their corresponding (bottom) color map for the normalized minor axis, where red colors represent positive minor axis (cyclonic rotation) and blue colors represent negative minor axis (anticyclonic rotation).

3.6 Rotary Spectra

The analysis showed a predominant clockwise rotation at the diurnal and semi-diurnal frequency for all seasons (Figure 28, a–f), common of the northern hemisphere, where inertial current rotate clockwise and tides have clockwise and counter-clockwise component. Although Rotary spectra are useful to separate the motions, given the local inertial period, it is hard to separate inertial motions from diurnal motions.

In limited cases (counterclockwise component of fall 2016 and 2017, and clockwise component of winter), the power content on the semidiurnal component was higher than that of the diurnal frequency.

Summer 2017 was the season with the greatest power content, with 112.7 (cm^2/s^2)/cpd on the clockwise component at the diurnal frequency, an order of magnitude above the corresponding semi-diurnal. Summer 2017 was followed by the summer 2016 and fall 2016, seasons that showed a similar spectral density, 68.2 and 58.62 (cm^2/s^2)/cpd, respectively, for the clockwise component at the diurnal frequency.

Spring 2017 and fall 2017 had a similar power content for the diurnal and semi-diurnal component of the clockwise and counterclockwise rotation, respectively. Only summer 2016 and fall2017 showed a slightly higher power content on the counterclockwise rotation at the semidiurnal frequency.

Winter 2016–2017 (Figure 28, a):

Clockwise	Counterclockwise
Diurnal density power: 25.37 (cm^2/s^2)/cpd	Diurnal density power: 6.92 (cm^2/s^2)/cpd
Semidiurnal density power: 32.14 (cm^2/s^2)/cpd	Semidiurnal density power: 20.59 (cm^2/s^2)/cpd

Spring 2017 (Figure 28, b):

Clockwise	Counterclockwise
Diurnal density power: 22.81 (cm^2/s^2)/cpd	Diurnal density power: 17.7 (cm^2/s^2)/cpd
Semidiurnal density power: 21.12 (cm^2/s^2)/cpd	Semidiurnal density power: 12.96 (cm^2/s^2)/cpd

Summer 2016 (Figure 28, c):

Clockwise	Counterclockwise
Diurnal density power: 68.2 (cm^2/s^2)/cpd	Diurnal density power: 29.1 (cm^2/s^2)/cpd
Semidiurnal density power: 14.12 (cm^2/s^2)/cpd	Semidiurnal density power: 15.64 (cm^2/s^2)/cpd

Summer 2017 (Figure 28, d):

Clockwise	Counterclockwise
Diurnal density power: 112.7 (cm^2/s^2)/cpd	Diurnal density power: 19.24 (cm^2/s^2)/cpd
Semidiurnal density power: 14.49 (cm^2/s^2)/cpd	Semidiurnal density power: 13.37 (cm^2/s^2)/cpd

Fall 2016 (Figure 28, e):

Clockwise	Counterclockwise
Diurnal density power: 58.62 (cm^2/s^2)/cpd	Diurnal density power: 9.67 (cm^2/s^2)/cpd
Semidiurnal density power: 19.32 (cm^2/s^2)/cpd	Semidiurnal density power: 16.88 (cm^2/s^2)/cpd

Fall 2017 (Figure 28, f):

Clockwise	Counterclockwise
Diurnal density power: 16.84 (cm^2/s^2)/cpd	Diurnal density power: 8.016 (cm^2/s^2)/cpd
Semidiurnal density power: 8.5 (cm^2/s^2)/cpd	Semidiurnal density power: 8.618 (cm^2/s^2)/cpd

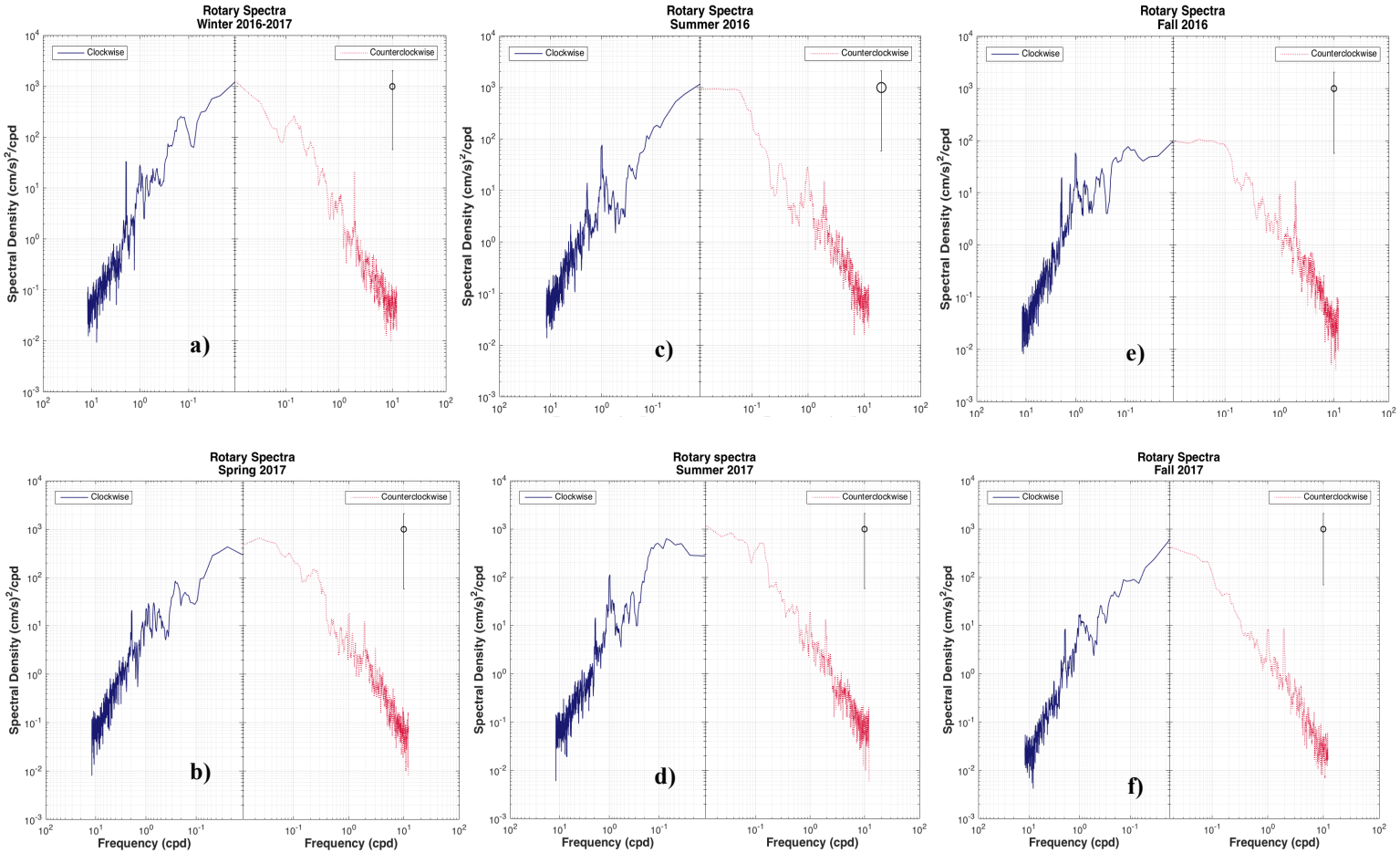

Figure 28. Rotary Spectra for a) Winter, b) Spring, c) Summer 2016, d) Summer 2017, e) Fall 2016, and f) Fall 2017. The left side of each panel represents the clockwise rotation and the right side represents the counterclockwise rotation. The 95% confidence interval is represented on the top right corner.

3.7 Wavelet Analysis

All the seasons were analyzed using wavelet analysis. However, it was expected to observe a persistent pattern of high power in the diurnal and semidiurnal frequency, but it was not detectable, and therefore the analysis for the full record was incorporated to detect the effect of diurnal and semi-diurnal tides. To contrast the previous dataset, wavelet analysis was performed on the full-detided record.

To reduce the variance a normalized time series is used to perform the analysis (panel a) on the subplots of Figure 29 A–H). The normalized time-series allows one to see prompt increases in the speed, mainly fronts or storm induced perturbations. Winter (Figure 29, A) shows an example of short-lived speed intensification in late January due to a frontal passage.

The oscillations on the time series have scales of variability associated with them. In short records of this data set, probably the most notorious scale of variability is the diurnal response due to tides. Nonetheless scales of variability range from high-frequency perturbations (more than twice a day) to weather band features (2-15 days). The panel b) on the subplots of Figure 29 A–H, shows the temporal evolution of different scales of variability. Yellow colors indicate higher power content. Note that yellow patches are more frequent in the 0.5-day scale (semi-diurnal oscillations) and 1 day scale (diurnal oscillations), with some patches on the low frequencies (weather band). Figure 29, G (full record) shows a strong banding in the diurnal and the semidiurnal frequency. When the record is detided (Figure 29, H) the semi-diurnal banding is vanished, however there is still some banding in the diurnal frequency. The diurnal banding is less intensified than in the raw record, but it is concentrated during the summers suggesting

that this is due to the inertial response to the sea-breeze effects enhanced by the local inertial period (24.78 hrs.).

The panel c) is a horizontal average of panel b), resulting in a global time-averaged power spectrum, and therefore the higher power content is found in the semi-diurnal, diurnal and weather band periods. Only winter and fall 2017 did not depict a clear peak for the semi-diurnal, and coincidently, these seasons showed the smallest power content on the diurnal period.

The maximum power for the diurnal frequency corresponded to summer 2017 (1111 cm^2/s^2). Spring 2017, summer 2016 and fall 2016 had a similar power content on the diurnal frequency (~690 cm^2/s^2). Summer 2016 presented the greatest power content for the semi-diurnal period (407.1 cm^2/s^2), followed by spring (348 cm^2/s^2).

Besides the maximum in the diurnal and semi-diurnal frequencies, there is high dominant power content peak in the low frequencies for all the seasons, except for the fall 2017, coinciding to the 9.3 days period for three of the season. In general, the high power band approximates the weather band (2 –15 days). High power in the weather band extends throughout the season during winter, summer 2016 and 2017, and fall 2017. During spring and fall 2016 the energy is localized in specific weeks of the season, as can be observed in Figure 29, B and E respectively.

Spring 2017 (Figure 29, B):

Diurnal power: 687.7 cm^2/s^2

Semidiurnal power: 348 cm^2/s^2

1st Maximum: 780.7 cm^2/s^2 at 3.9-day period

3rd Maximum: 427.3 cm^2/s^2 at 9.3-day period

High power band: 2.7–5.5 days

Summer 2016 (Figure 29, C):

Diurnal power: 689.8 cm^2/s^2

Semidiurnal power: 407.1 cm^2/s^2

2^{nd} Maximum: 561.3 cm^2/s^2 at 13.1-day period

High power band: 13.10–15.5 days

Summer 2017 (Figure 29, D)

Diurnal power: 1111 cm^2/s^2

Semidiurnal power: 253.7 cm^2/s^2

1^{st} Maximum: 1597 cm^2/s^2 at 9.3-day period

High power band: 4.6–15.5 days

Fall 2016 (Figure 29, E):

Diurnal power: 697.4 cm^2/s^2

Semidiurnal power: 245.8 cm^2/s^2

1^{st} maximum: 514.1 cm^2/s^2 at 9.3-day period

High power band: 5.5 –15.5 days

Winter (Figure 29, A):

Diurnal power: 372 cm^2/s^2

1^{st} Maximum: 1781 cm^2/s^2at 7.8-day period

High power band: 2.3–11.1 days

Fall 2017 (Figure 29, F):

Diurnal power: 399.6 cm^2/s^2

High power band: 0.8 –3.2 days

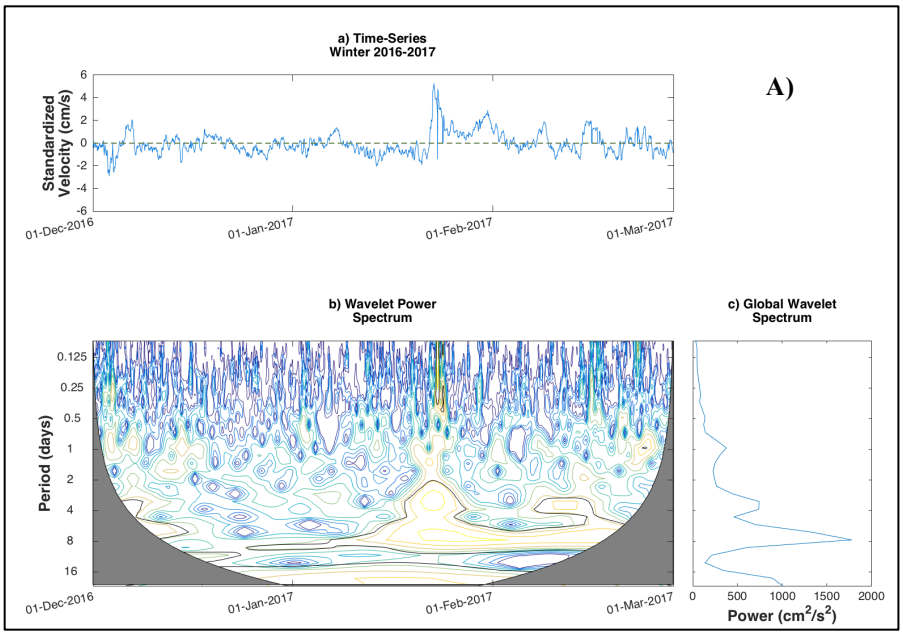

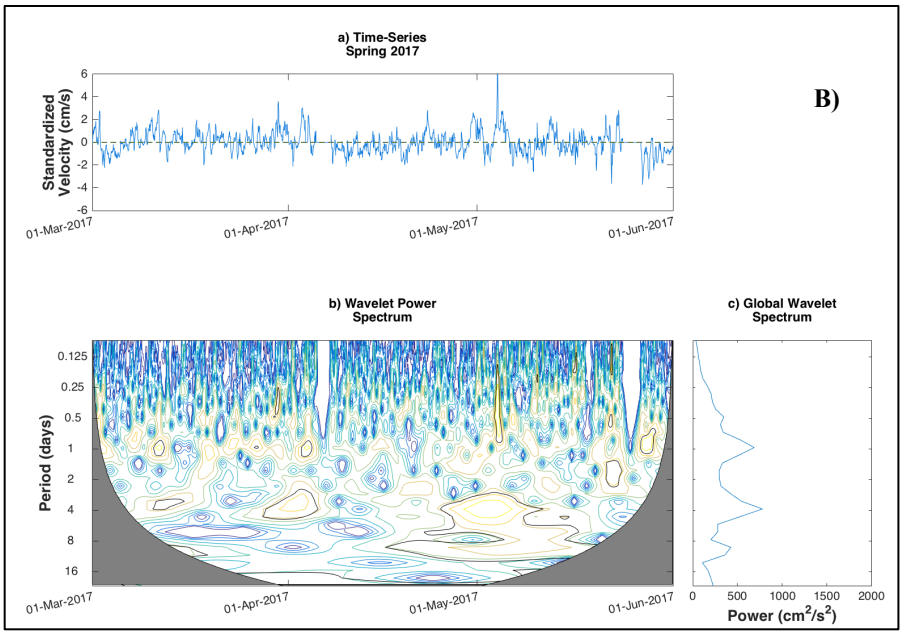

Figure 29. (a) Standardized alongshore velocity for A) Winter, B) Spring, C) Summer 2016, D) Summer 2017, E) Fall 2016, F) Fall 2017, G) Full record, and H) Full detided. (b) Local rectified wavelet power spectrum of (a), using the Morlet wavelet normalized by $1/s^2$; the x-axis is time, and the y-axis is the Fourier period (days). The thick contour encloses regions of confidence greater than 95%. The gray patch delimits the cone of influence. (c) Rectified time-average power spectrum.

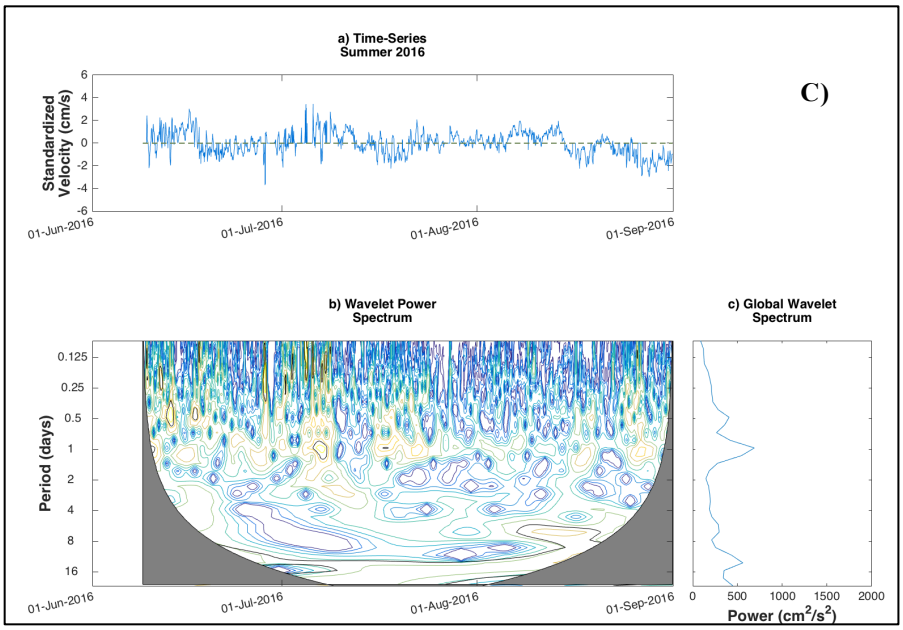

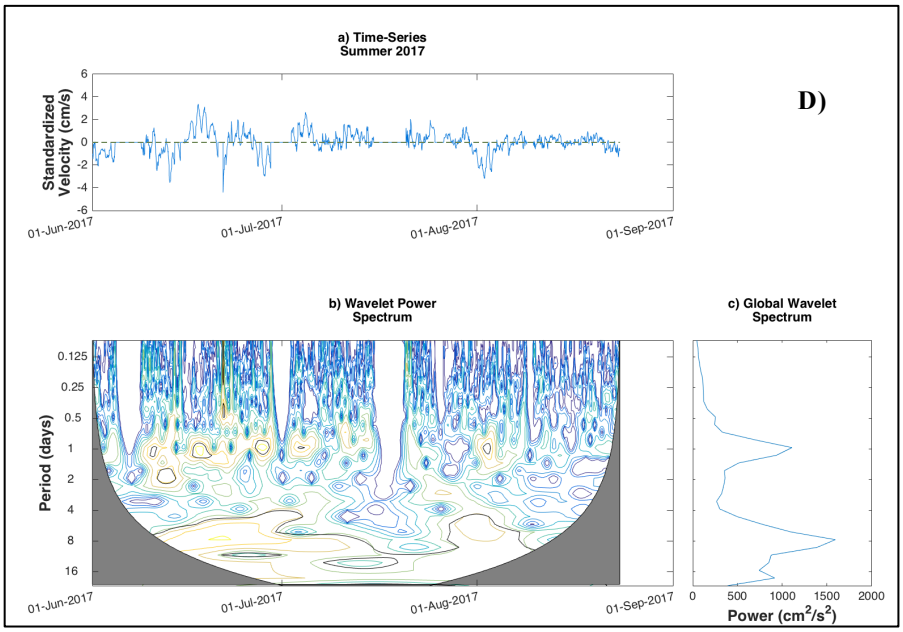

Figure 29. Continued.

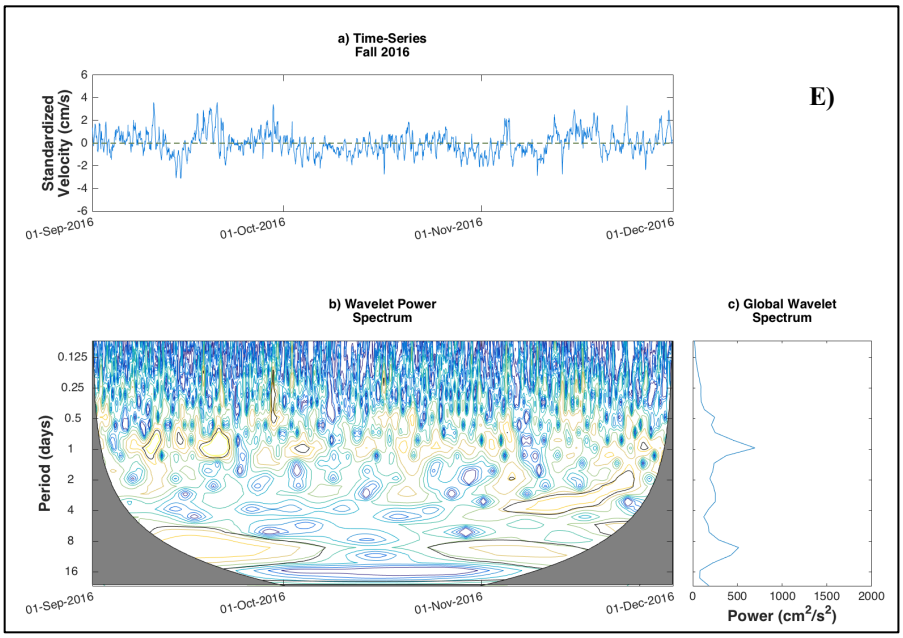

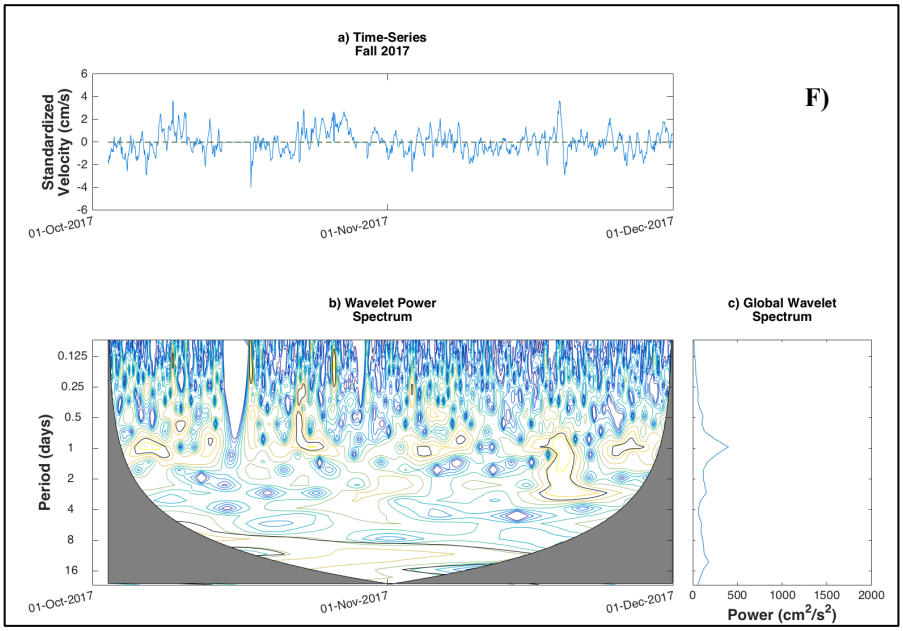

Figure 29. Continued.

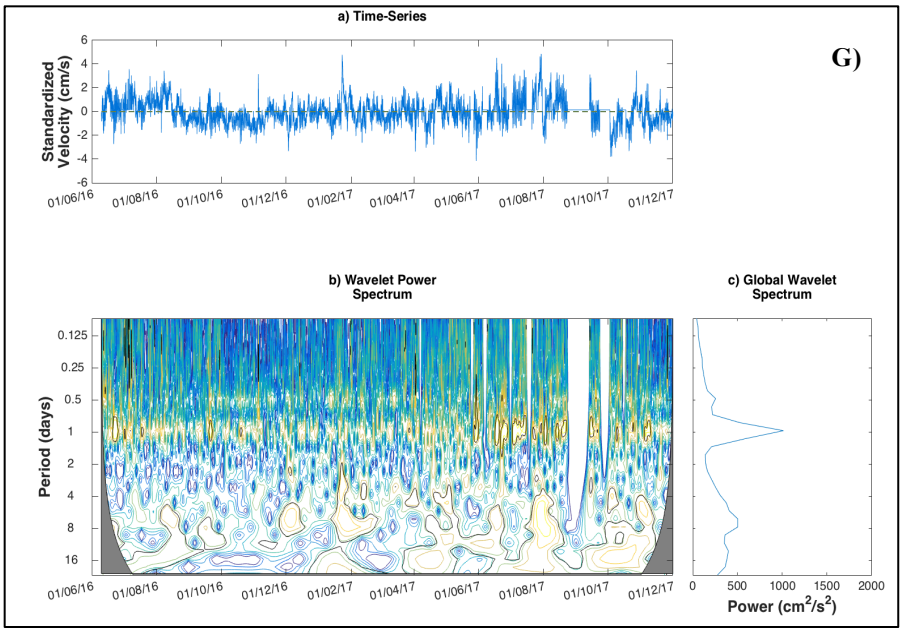

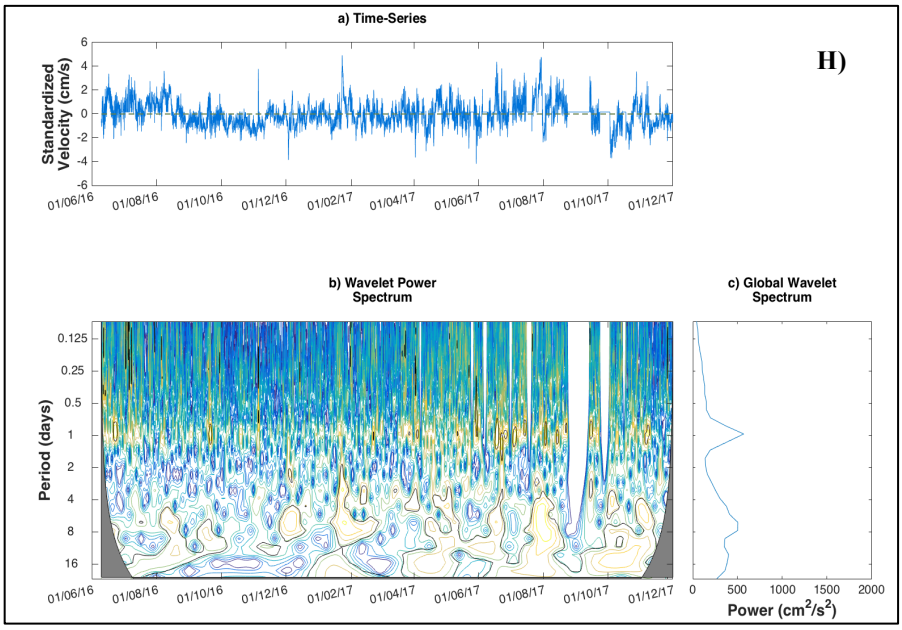

Figure 29. Continued.

3.8 Coherence

Coherence quantifies the correlation in frequency between the alongshore and cross-shore component. The top panel of the Figure 30, a-f, shows the coherence between both components as a function of frequency, ranging from 0-1, where 1 indicates the highest coherence. The red dashed line represents the 95% confidence interval; anything below that 95% confidence interval is not coherent. There is phase associated with each calculation of coherence. The bottom panel in Figure 30, a-f, only shows the phase when the coherence is above the 95% interval. A positive phase indicates that the alongshore component leads the cross-shore component. The high frequencies are outside the scope of this thesis, and therefore they were neglected and patched in gray.

Coherence above the 95% confidence interval was observed near the inertial and semi-diurnal period, but predominantly in the inertial period, with the cross-shore leading the alongshore component, indicative of rotation due to inertial response.

For the winter (Figure 30, a) at the near-inertial frequency (0.93 cpd with $\gamma^2 = 0.84$) the cross-shore component lead the alongshore component by -100º, equivalent to 6.6 hours. Near the semi-diurnal period (1.875 cpd with $\gamma^2 = 0.55$), the cross-shore component led the alongshore component by -143º, comparable to 9.5 hours.

During the spring (Figure 30, b) a nearly in-phase (-167.5º) peak at 1.969 cpd outstood from the record, with a coherence of $\gamma^2 = 0.74$, where the cross-shore component led the alongshore component for 11.1 hours.

Summer of 2016 (Figure 30, c) presented peaks above the 95% confidence interval for frequencies below 1 cpd with the greatest coherence, $\gamma^2 = 0.82$, localized in-phase at 0.18 cpd

During the summer of 2017 (Figure 30, d), the greatest coherence was $\gamma^2 = 0.72$, corresponding to the near-inertial frequency (0.93 cpd), with a phase of -125º, meaning that the along-shore component lagged 8 hours the cross-shore circulation.

Fall of 2016 (Figure 30, e) expressed high coherence for the diurnal ($\gamma^2 = 0.75$) and semi-diurnal frequency ($\gamma^2 = 0.59$), 1.031 cpd and 1.969 cpd, respectively. In both cases, the alongshore component lagged the cross-shore component by 6.3 and 11.6 hours, respectively, with corresponding phases of -95º and -175º, indicative of a nearly in-phase relationship on the semi-diurnal frequency.

For the fall of 2017 (Figure 30, f) the maximum coherence, $\gamma^2 = 0.63$, happened during the semi-diurnal frequency (1.969 cpd), where the alongshore and cross-shore component were in phase, with the cross-shore component leading the alongshore component for 12 hours.

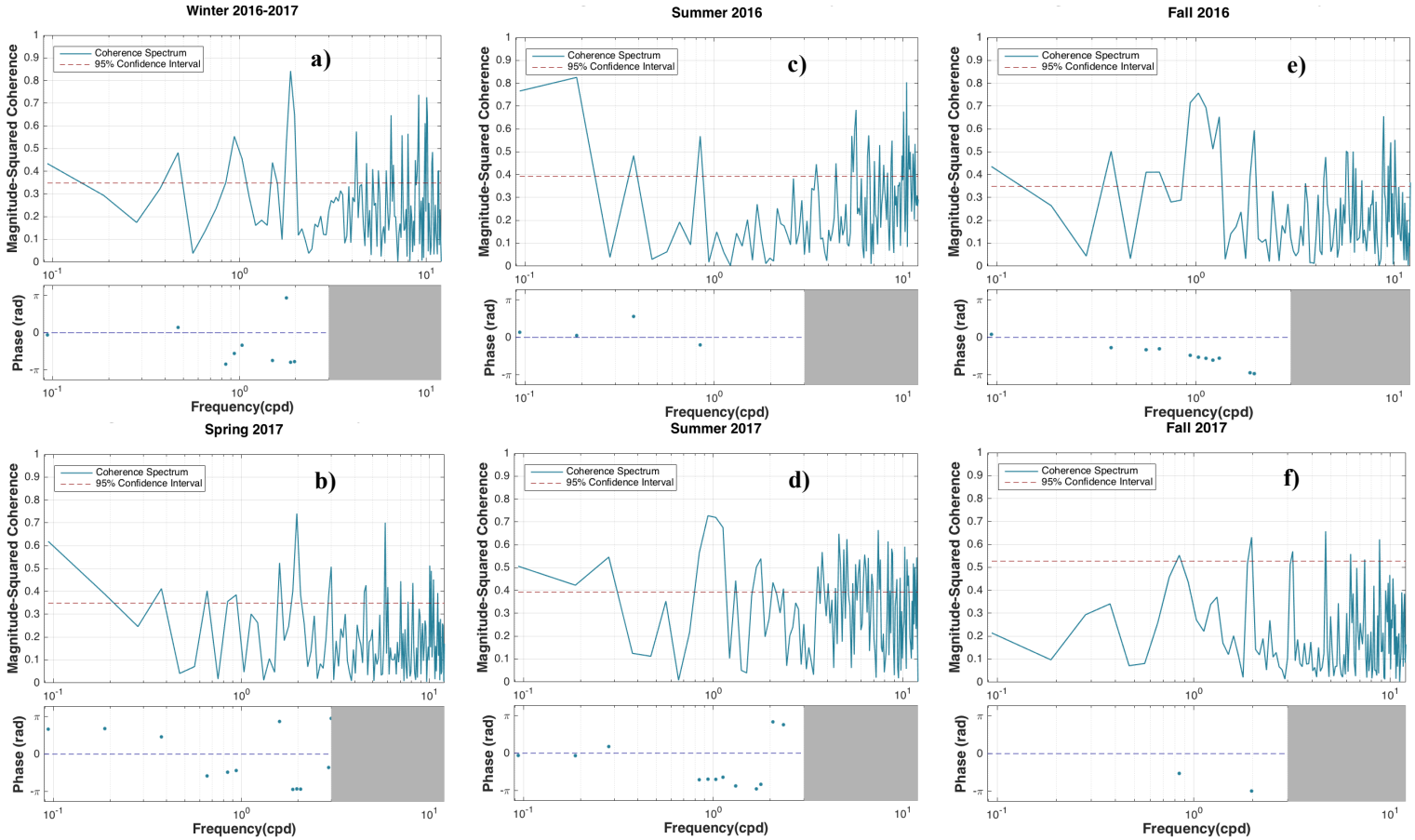

Figure 30. (Top) Alongshore and cross-shore magnitude-squared coherence spectra, with the 95% confidence interval indicated with a red dashed line, for a) Winter, b) Spring, c) Summer 2016, d) Summer 2017, e) Fall 2016, and f) Fall 2017. (Bottom) Phase in radians, where the gray patch indicates the area where the changes in phase are being neglected for the same seasons (a–f).

4. DISCUSSION

The assessment of the performance of the HF radar shows that SSDE performs better than RLVR, and that both systems correlate better when comparing with buoy F, due to the centric location of this buoy within the HF radar footprint and the high amount of data collected on that region by the HF radar. For RLVR, summer 2016 has the greatest correlation coefficient. For SSDE, winter has the greatest correlation coefficient. The satisfactory performance during summer 2016 is attributed to the saline water brought by the upcoast circulation, while during the winter there is low freshwater content, potentially improving the response of the HF radar system. Summer 2016 (0.75), spring (0.79) and winter (0.87) have the greatest correlation coefficients observed through the record. Minimum, maximum and mean values of the buoy data projected along the radials compared to the radial data are similar, and therefore, the speeds measured with each sensor results in similar frequency histograms. The values from both systems are, in general, within less than one standard deviation. The greatest speed values captured during the time series analyzed correspond to the summer with some intensification during the winter due to frontal passages.

Some factors interfering with the performance of the HF radar are nearby oil and gas platforms, communications systems of vessels traveling in the surrounding waterways, and also, the signal could be attenuated by changes in the atmospheric refraction index, but these atmospheric changes are not addressed in this thesis.

Variance ellipses show a predominant NE-SW direction for all the season, reflecting the dominant wind-driven alongshore flow. Variance ellipses tend to follow the

50-m isobath in agreement to the inshore-offshore 50-m isobath limit definition by Nowlin et al. (2005). Due to the increase in the speed, the exacerbation of the sea-breeze due to land-water temperature gradients, and the circulation reversal, summer is the season that traced the biggest variance ellipses. Variance increases in those regions where fewer data was measured and where there are steeper gradients in the bathymetry. Ellipses near the shore are anisotropic with a cross-shore pattern due to the near parallel incidence angle between radials from SSDE and RLVR. There are some elongated ellipses close to RLVR with an N-S to cross-shore orientation, related to the faster decrease in the signal intensity observed in RLVR compared to SSDE. There might be a contribution on the incidence angles due to the curvature of the coastline. Fall 20l6/2017 are the seasons with the least variance due to the uniform distribution of the isohalines about the isobaths. Fall is the season with the smallest freshwater, and therefore, fall of 2016 is the season with the maximum data available and smallest variance. Winter is the second season with the least variance; reasons for this low variance are that winter is one of the seasons with the most data available and that during winter there are not strong sea-breeze effects. The presence of frontal passages during winter, make it have higher variability compared to the fall 2016/2017. Spring is the season with the smallest salinity, and given that the radar responds to changes in salinity, this season presents the steepest gradients in data availability and high variability on the variance ellipse distribution.

Power spectra analysis reveals dominant power spectral density at 1 and 2 cpd with a predominant clockwise rotation, with few cases of dominant counter-clockwise rotation, revealed by rotary analysis. The increase in power in the diurnal and semi-diurnal frequencies is a result of the tidal response. Summer shows the greatest energy

content, predominantly in the cross-shore component. The low-frequency slope of the power spectra approximates the theoretical energy cascade decade (Kolmogorov -5/3 law).

In agreement to DiMarco and Reid (1998), the main tidal constituents are O1, P1, K1, M2, and S2, with a predominant anticyclonic rotation, except for M2 that shows a dominant cyclonic rotation along the coast. Diurnal ellipses trace ellipses with a characteristic circular shape, and the semi-diurnal constituents trace ellipses with an elongated shape. The power content of P1 decreases when summers are removed from the record, potentially associated with a summer intensification due to the near-resonant response to the sea-breeze at the given local inertial period. The inertial period for this region ranges from 24.367–25.31 hrs., with a local inertial period of 24.78 hrs. for the HF radar data point with the most data collected, and used for tidal analysis and wavelet analysis.

Wavelet analysis shows an increase in the energy content for the diurnal and semi-diurnal frequency, and the temporal distribution of the energy content show an increase of energy content on the weather-band (2-15 days). However, the diurnal band is not perceptible on the seasonal plot but in the full data set. When removing the tides from the full dataset there is no high power content in the semi-diurnal period, but there is some high energy content on the diurnal band during the summers as a result of the sea-breeze effect that is enhanced during this season.

Coherence above the 95% confidence interval is observed in the inertial band, with the cross-shore (alongshore) component leading (lagging) the alongshore (cross-shore) component, indicative of rotation due to inertial response.

5. CONCLUSIONS

Having the HF radar on the Texas coast enhances the spatial coverage, and although the mechanisms to collect data from these systems imply different principles of operation, the HF radar and TABS buoys supplement each other. Each system offers different capabilities, and therefore, it is necessary to keep both systems integrated to have a comprehensive ocean observing systems on the Texas coast to ease the decision-making process of the responders and mitigate further social, economic and environmental damage to the coastal locations.

A potential future direction of the applications of the HF radar is to integrate the outputs from the radar on an ocean circulation model and design a particle tracking system. For future incorporation of the data into models, it is necessary to perform the proper quality assurance and quality control (QA/QC) procedure of the data collected. Also, it is fundamental to consider that the variance close to the shore (baseline) and on the edges of the HF radar footprint are not a contribution of the coastal circulation, but a result of the coastal geometry and the angle formed between the beams from both HF radar systems. Therefore, it is essential to take into account the geometric limitations that come with the system.

Some recommendations to improve the data collected by the HF radar include calibrating the antenna to reduce interference from surroundings, increasing the distance between the transmitter, receiver, and electronics trailer to reduce signal contamination as well as keeping a digital log of each site.

REFERENCES

Athié, G., Sheinbaum, J., Leben, R., Ochoa, J., Shannon, M., & Candela, J. (2015). Interannual variability in the Yucatan Channel flow. *Geophysical Research Letters, 42*, 1496-1506

Barrick, D. (1972). Remote sensing of sea state by radar. In, *Engineering in the Ocean Environment, Ocean 72-IEEE International Conference on* (pp. 186-192): IEEE

Barrick, D.E., Evans, M., & Weber, B. (1977). Ocean surface currents mapped by radar. *Science, 198*, 138-144

Barron, C.N., & Vastano, A.C. (1994). Satellite observations of surface circulation in the northwestern Gulf of Mexico during March and April 1989. *Continental Shelf Research, 14*, 607-628

Bender, L., Guinasso, N., Walpert, J.N., Lee, L., Martin, R.D., Hetland, R.D., Baum, S.K., & Howard, M.K. (2007). Development, operation and results from the Texas Automated Buoy System. *Gulf of Mexico Science, 25*, 33

Biggs, D., Fargion, G., Hamilton, P., & Leben, R. (1996). Cleavage of a Gulf of Mexico Loop Current eddy by a deep water cyclone. *Journal of Geophysical Research: Oceans, 101*, 20629-20641

Bloomfield, P. (1976). Fourier analysis of time series: an introduction. *Wiley Series in Probability and Mathematical Statistics, New York: Wiley, 1976*

Chen, C., Reid, R.O., & Nowlin, W.D. (1996). Near-inertial oscillations over the Texas-Louisiana shelf. *Journal of Geophysical Research: Oceans, 101*, 3509-3524

Cho, K., Reid, R.O., & Nowlin, W.D. (1998). Objectively mapped stream function fields on the Texas-Louisiana shelf based on 32 months of moored current meter data. *Journal of Geophysical Research: Oceans, 103*, 10377-10390

Cochrane, J., & Kelly, F. (1986). Low-frequency circulation on the Texas-Louisiana continental shelf. *Journal of Geophysical Research: Oceans, 91*, 10645-10659

Cushman-Roisin, B., & Beckers, J.-M. (2011). *Introduction to geophysical fluid dynamics: physical and numerical aspects*. Academic Press

DiMarco, S.F. (1998). On the use of the method of cyclic descent to estimate principal tidal constituents from oceanographic time-series. *LATEX Shelf Technical Report, 98-1-T*

DiMarco, S.F., Howard, M.K., & Reid, R.O. (2000). Seasonal variation of wind-driven diurnal current cycling on the Texas-Louisiana Continental Shelf. *Geophysical Research Letters, 27*, 1017-1020

DiMarco, S.F., & Reid, R.O. (1998). Characterization of the principal tidal current constituents on the Texas-Louisiana shelf. *Journal of Geophysical Research: Oceans, 103*, 3093-3109

DiMego, G.J., Bosart, L.F., & Endersen, G.W. (1976). An examination of the frequency and mean conditions surrounding frontal incursions into the Gulf of Mexico and Caribbean Sea. *Monthly weather review, 104*, 709-718

Dinnel, S., & Wiseman, W.J. (1986). Fresh water on the Louisiana and Texas shelf. *Continental Shelf Research, 6*, 765-784

Donohue, K.A., Watts, D., Hamilton, P., Leben, R., & Kennelly, M. (2016). Loop current eddy formation and baroclinic instability. *Dynamics of Atmospheres and Oceans, 76*, 195-216

Etter, P.C., Howard, M.K., & Cochrane, J.D. (2004). Heat and freshwater budgets of the Texas-Louisiana shelf. *Journal of Geophysical Research: Oceans, 109*

Godin, G. (1972). The analysis of tides, 264 pp. *University of Toronto*

Gonella, J. (1972). A rotary-component method for analysing meteorological and oceanographic vector time series. In, *Deep Sea Research and Oceanographic Abstracts* (pp. 833-846): Elsevier

Guinasso, N.L., Yip, J., Reid, R., Bender, L., Howard, M., Lee, L., Walpert, J., Brooks, D., Hetland, R., & Martin, R. (2001). Observing and Forecasting Coastal Currents: Texas Automated Buoy System (TABS). In, *OCEANS, 2001. MTS/IEEE Conference and Exhibition* (pp. 1318-1322): IEEE

Gurgel, K.-W., Essen, H.-H., & Kingsley, S. (1999). High-frequency radars: physical limitations and recent developments. *Coastal Engineering, 37*, 201-218

Harlan, J., Terrill, E., Hazard, L., Keen, C., Barrick, D., Whelan, C., Howden, S., & Kohut, J. (2010). The integrated ocean observing system high-frequency radar network: status and local, regional, and national applications. *Marine Technology Society Journal, 44*, 122-132

Howden, S.D., Barrick, D., & Aguilar, H. (2011). Applications of high frequency radar for emergency response in the coastal ocean: utilization of the Central Gulf of Mexico Ocean Observing System during the Deepwater Horizon oil spill and vessel tracking. In, *SPIE Defense, Security, and Sensing* (pp. 80300O-80300O-80310): International Society for Optics and Photonics

Kowalik, Z., & Luick, J. (2013). The Oceanography of Tides. *Ch, 1*, 5-14

Li, Y., Nowlin, W., & Reid, R. (1997). Mean hydrographic fields and their interannual variability over the Texas-Louisiana continental shelf in spring, summer, and fall. *Journal of Geophysical Research: Oceans, 102*, 1027-1049

Li, Y., Nowlin, W.D., & Reid, R.O. (1996). Spatial-scale analysis of hydrographic data over the Texas-Louisiana continental shelf. *Journal of Geophysical Research: Oceans, 101*, 20595-20605

Liu, Y., San Liang, X., & Weisberg, R.H. (2007). Rectification of the bias in the wavelet power spectrum. *Journal of Atmospheric and Oceanic Technology, 24*, 2093-2102

Mooers, C.N. (1973). A technique for the cross spectrum analysis of pairs of complex-valued time series, with emphasis on properties of polarized components and rotational invariants. In, *Deep Sea Research and Oceanographic Abstracts* (pp. 1129-1141): Elsevier

Morey, S.L., Martin, P.J., O'Brien, J.J., Wallcraft, A.A., & Zavala-Hidalgo, J. (2003). Export pathways for river discharged fresh water in the northern Gulf of Mexico. *Journal of Geophysical Research: Oceans, 108*

Nowlin, W., Jochens, A., Reid, R., & DiMarco, S. (1998). Texas–Louisiana shelf circulation and transport processes study: synthesis report. *Volume II: Appendices. US Dept. of the Interior, Minerals Management Services, Gulf of Mexico OCS Region, New Orleans, LA. OCS Study MMS*, 98-0036

Nowlin, W.D. (1968). A detached eddy in the Gulf of Mexico. *J. Mar. Res., 26*, 185-186

Nowlin, W.D. (1971). Water masses and general circulation of the Gulf of Mexico. *OCEANOLOGY, VOL 6, NO 2, P 28-33, FEBRUARY, 1971. 6 P, 15 FIG.*

Nowlin, W.D., Jochens, A.E., DiMarco, S.F., Reid, R.O., & Howard, M.K. (2005). Low-frequency circulation over the Texas-Louisiana continental shelf. *Circulation in the Gulf of Mexico: Observations and models*, 219-240

Oey, L.Y., Ezer, T., & Lee, H.C. (2005). Loop Current, rings and related circulation in the Gulf of Mexico: A review of numerical models and future challenges. *Circulation in the Gulf of Mexico: Observations and models*, 31-56

Paduan, J.D., & Graber, H.C. (1997). Introduction to high-frequency radar: reality and myth. *Oceanography, 10*, 36-39

Reid, R.O., & Whitaker, R.E. (1981). *Numerical model for astronomical tides in the Gulf of Mexico*. Texas A & M University, Department of Oceanography

Roarty, H., Glenn, S., Kohut, J., Gong, D., Handel, E., Rivera, E., Garner, T., Atkinson, L., Brown, W., & Jakubiak, C. (2010). Operation and application of a regional high-frequency radar network in the Mid-Atlantic Bight. *Marine Technology Society Journal, 44*, 133-145

Schmitz, W., Biggs, D., Lugo-Fernandez, A., Oey, L.Y., & Sturges, W. (2005). A synopsis of the circulation in the Gulf of Mexico and on its continental margins. *Circulation in the Gulf of Mexico: Observations and models*, 11-29

Smith, N.P. (1980). Temporal and spatial variability in longshore motion along the Texas Gulf coast. *Journal of Geophysical Research: Oceans, 85*, 1531-1536

Sturges, W., & Leben, R. (2000). Frequency of ring separations from the Loop Current in the Gulf of Mexico: A revised estimate. *Journal of Physical Oceanography, 30*, 1814-1819

Teague, C.C., Vesecky, J.F., & Fernandez, D.M. (1997). HF radar instruments, past to present. *Oceanography, 10*, 40-44

Thompson, R.O. (1979). Coherence significance levels. *Journal of the Atmospheric Sciences, 36*, 2020-2021

Thomson, R.E., & Emery, W.J. (2014). *Data analysis methods in physical oceanography*. Newnes

Torrence, C., & Compo, G.P. (1998). A practical guide to wavelet analysis. *Bulletin of the American Meteorological society, 79*, 61-78

Walpert, J.N., Guinasso, N.L., Lee, L.L., & Martin, R.D. (2011). Texas Automated Buoy System-sustainable ocean observations to help protect the environment. In, *OCEANS'11 MTS/IEEE KONA* (pp. 1-7): IEEE

Wang, W., Nowlin, W.D., & Reid, R.O. (1998). Analyzed surface meteorological fields over the northwestern Gulf of Mexico for 1992-94: Mean, seasonal, and monthly patterns. *Monthly weather review, 126*, 2864-2883

Welch, P. (1967). The use of fast Fourier transform for the estimation of power spectra: a method based on time averaging over short, modified periodograms. *IEEE Transactions on audio and electroacoustics, 15*, 70-73

Zarate, L., DiMarco, S., Knap, A., Walpert, J., & Whilden, K. (2016). A high-frequency radar oceanic current monitoring system for the Texas coast. In, *OCEANS 2016 MTS/IEEE Monterey* (pp. 1-7): IEEE

Zavala-Hidalgo, J., Morey, S., O'BRIEN, J., & Zamudio, L. (2006). On the Loop Current eddy shedding variability. *Atmósfera, 19*, 41-48

Zetler, B., & Hansen, D. (1970). Tides in the Gulf of Mexico—A review and proposed program. *Bulletin of Marine science, 20*, 57-69

Zhang, X., DiMarco, S.F., Smith IV, D.C., Howard, M.K., Jochens, A.E., & Hetland, R.D. (2009). Near-resonant ocean response to sea breeze on a stratified continental shelf. *Journal of Physical Oceanography, 39*, 2137-2155

Websites

AANDERAA Instruments. DCS Operation Manual
Available at http://www.aanderaa.com/media/pdfs/dcs-4100-4100r.pdf.
Last date accessed: 30 May 2018

BOEM. Oil and Gas Leasing on the Outer Continental Shelf. Department of the Interior.
Available at http://www.boem.gov/uploadedFiles/BOEM/Oil_and_Gas_Energy_Program/Leasing/5BOEMRE_Leasing101.pdf.
Last date accessed: 18 November 2016.

Codar Ocean Sensors
Available at http://codar.com
Last date accessed: 30 May 2018.

Gulfbase. Tourism
Available at https://www.gulfbase.org/environmental-issue/tourism
Last date accessed: 30 May 2018.

Manual For Real-time Quality Control Of High Frequency Radar Surface Current Data
Available at https://ioos.noaa.gov/ioos-in-action/manual-real-time-quality-control-high-frequency-radar-surface-current-data/
Last date accessed: 30 May 2018

NOAA Physical Oceanography Division
Available at http://www.aoml.noaa.gov/phod/dhos/altimetry.php.
Last date accessed: 30 May 2018

The U.S. Integrated Ocean Observing System
Available at https://ioos.noaa.gov/
Last date accessed: 30 May 2018.

ST, NOAA (Office of Science and Technology) Gulf of Mexico Regional Summary.
Available at
https://www.st.nmfs.noaa.gov/Assets/economics/documents/feus/2011/FEUS2011%20-%20Gulf%20of%20Mexico.pdf
Last date accessed: 30 May 2018.

Rutgers. HF radar
Available at https://marine.rutgers.edu/cool/education/spring2000/kristiea/project1.html
Last date accessed: 30 May 2018.

Wavelet analysis software. University of Colorado Boulder.
Available at http://paos.colorado.edu/research/wavelets/software.html
Last date accessed: 30 May 2018.

Data Sets

National HF RADAR Network. Surface Currents
Available at http://cordc.ucsd.edu.
Last date accessed: 30 May 2018.

Texas Automated Buoy System, Gulf Of Mexico Ocean Observatory, Texas Coastal Ocean Observation, Real Time Oceanographic Data Supporting Oil Spill Prevention And Response.
Available at http://tabs.gerg.tamu.edu
Last date accessed: 30 May 2018.